Chemical Geology 322-323 (2012) 47–67

Contents lists available at SciVerse ScienceDirect

Chemical Geology

journal homepage: www.elsevier.com/locate/chemgeo

Deformation-related alteration of basaltic clasts during deep burial in sedimentary basins

Benjamin Malvoisin [a,*], Håkon Austrheim [b], Anders Malthe-Sørenssen [b], Johannes Glodny [c]

[a] Ecole normale supérieure, Laboratoire de Géologie, Paris, France
[b] Physics of Geological Processes, University of Oslo, Norway
[c] Deutsches GeoForschungsZentrum (GFZ), Potsdam, Germany

ARTICLE INFO

Article history:
Received 25 January 2012
Received in revised form 26 May 2012
Accepted 12 June 2012
Available online 20 June 2012

Editor: J.D. Blum

Keywords:
Basaltic clasts
Alteration
Devonian Solund basin
Reaction–diffusion process
Chemical and mechanical compaction
CO_2-sequestration

ABSTRACT

The once deeply buried conglomerates of the Solund basin contain up to 30% basaltic clasts together with up to 20% altered peridotite clasts, both derived from the adjacent Solund-Stavfjord Ophiolite Complex (SSOC). The basaltic clasts range in size from 2 to 30 cm across and display centimeter-thick hematite reddened zones. Four types which form an alteration-related evolutionary sequence can be distinguished. Type 1 consists of a green core with a 1–2 cm thick red zone along its rim. Type 2 shows, in addition, a perturbation of the red zone into the center of the clasts. In Type 3, numerous compartments with green cores surrounded by red zones build up the clast. Type 4 displays diffuse red zones and patches typically with a circular form that resembles Liesegang's structures. This evolutionary sequence relates to a progressive deformation evident from fractures, faults and shear zones. Hematite reddened zones form along clast boundaries and along fractures that are oriented at high angle to the boundaries of the clasts. The boundary-parallel zones migrate towards the center of the clasts and the fracture-parallel zones migrate away from the fractures. These fracturing and deformation are coupled with chemical and mineralogical changes responsible of the changes in color of the alteration zones. Compared to the basaltic rocks of the SSOC, the basaltic clasts of the Solund basin contain higher contents of K_2O, volatiles (LOI) and MgO, lower contents of CaO and are more oxidized with an average $Fe^{3+}/(Fe^{3+}+Fe^{2+})$ ratio of 0.43 ($\pm$0.10) as compared to 0.30 ($\pm$0.07) in the SSOC basalts. The replacement of magmatic clinopyroxene by chlorite induces the decrease in CaO. The replacement of ilmenite by titanite provides iron to form hematite in the red zones. The red zones progressively replace the green core and are, at their external boundary, in turn replaced by Mg-riched green alteration zones characterized by a high content of zoned amphibole. A decrease in CaO and an increase in MgO towards the rim of the basaltic clasts is contrary to the chemical evolution of the peridotite clasts, where the MgO is depleted and the CaO increases with increasing degree of alteration. This suggests that clasts of different lithologies exchanged components during the alteration process. To explain these observations, we use a model including internal stresses through a diffusion–reaction process and external stresses through sediment loading and tectonic forces. The mineralogy of the altered basaltic clasts (chlorite, epidote, albite, actinolite) corresponds to low-grade metamorphic conditions in accordance with or slightly higher than the peak temperature of 230–320 °C previously calculated for this basin. The study shows that the final compaction of multicomponent clast systems takes place through an interaction between mineral reactions, metasomatism and deformation, which differs from the compaction of monocomponent systems that occurs dominantly through pressure solution.

1. Introduction

The mineralogical and chemical changes that occur in sediments during burial will influence their petrophysical properties such as porosity, seismic velocity, density and thermal conductivity. Thus, these changes have to be precisely known to estimate the capacity of a rock as a reservoir for hydrocarbons (porosity) or to interpret seismic data (seismic velocity, density). The changes in petrophysical properties resulting from mineralogical and chemical changes are also very important input parameters in any numerical modeling of basin evolution and it is therefore necessary to assess also the rate of the alteration process.

During burial, the mineralogical and chemical changes will depend on parameters like temperature, fluid composition, or pressure and their evolution through time. The study of such changes can consequently provide constraints on the structural evolution of the basin. The reactivity of the clasts in a sedimentary basin is also important in the context of CO_2 sequestration. A permanent storage of CO_2, pumped into a sedimentary basin as suggested by the Intergovernmental Panel

* Corresponding author at: ISTerre, Maison des Géosciences BP 53, F-38041 Grenoble cedex 9, France.
E-mail address: benjamin.malvoisin@ujf-grenoble.fr (B. Malvoisin).

0009-2541/$ – see front matter © 2012 Elsevier B.V. All rights reserved.
doi:10.1016/j.chemgeo.2012.06.011

of Climate Change (IPCC), will require mineral reactions, like the fixation of CO_2 in carbonates as described in Beinlich et al. (2010). Ultramafic rocks and basalts are rock types actually discussed as potential targets for CO_2 sequestration (Kelemen and Matter, 2008; Gislason et al., 2010; Gysi and Stefánsson, 2011; Wolff-Boenisch et al., 2011; Rosenbauer et al., 2012). Their co-occurrence and close spatial relationships in the Solund basin allows an estimate of their relative reactivity in presence of CO_2 at depth in a sedimentary basin.

The burial-related changes occurring in near mono-component systems like sandstones and carbonates are known from theoretical studies (Audet and Fowler, 1992; Renard et al., 1999; Wenwu et al., 2003) experiments (Hickman and Evans, 1995; David et al., 2001; Zubtsov et al., 2004), simulations (Bakke and Øren, 1997; Lander and Walderhaug, 1999; Bernabé and Evans, 2007) and field studies (Dickinson and Milliken, 1995). However there are basins where the clast population is composed of mixtures of clasts of different multi-mineral source rocks (like peridotite + basalt + greywacke). Data on the evolution of such systems during burial are sparse or lacking. However, Benson and Teague (1982) have documented mineralogical and chemical changes during the burial of basalts to depths down to 1500 m. Beinlich et al. (2010) find that during burial and weathering the peridotitic clasts of the Solund basin (Western Norway) experienced strong chemical alteration (metasomatism) through reaction with basinal brines. Extreme removal of Mg (from 40 to 3 wt.% MgO) results in formation of quartz and of a secondary porosity. Calcite fills this porosity, resulting in an alteration product consisting of calcite, silica and hematite with only minor Mg-silicates. The field data are supported by experimental work of Hövelmann et al. (2011) which also suggests that alteration of olivine, through the alteration products it provides and the serpentine mesh texture it forms, enhances the carbonation rate. In this study, the authors point out that calcite forms at the site of the weathered olivine. The above studies of the ultramafic clasts suggest that such multi-component ultramafic clast-bearing systems will compact by processes other than pressure solution. Moreover, Ca required to form the carbonate must be derived from outside suggesting interaction with nearby Ca bearing clasts.

In this work, we focus on alteration of conglomerate boulders of basaltic composition found side by side with ultramafic clasts described by Beinlich et al. (2010). Like the ultramafic clasts of the Solund basin, the basaltic clasts display red alteration zones around fractures. The characterization of the mineralogical and chemical changes occurring during the alteration allows us to propose a chemical model for the alteration. The identification of the interplay of these changes with deformation in the clasts permit to qualitatively constrain the physical mechanisms driving progressive alteration.

2. Geological setting

2.1. The Devonian basins

The Solund basin (Kolderup, 1926) outcrops on several islands and is one of five continental Devonian Basins situated along the coast of W Norway (Fig. 1). The basins formed in response to late- or post-orogenic extension above an array of steep normal faults and low-angle extensional detachments (Hossack and Cooper, 1986; Osmundsen et al., 1998). The dominant extensional structure is the Nordfjord-Sogn detachment zone (Hossack, 1984). The Devonian basins (Hornelen, Haasteinen, Kvamshesten, Solund and Fensfjorden) are positioned in the hanging wall of normal faults and in the synforms of the detachment surface (Osmundsen and Andersen, 2001; Fig. 1b and c). The Solund basin fill rests, with a well preserved primary transgressive unconformity, on the Solund-Stavfjord ophiolite complex (SSOC) and associated metasedimentary and metavolcanic complexes in the north (Furnes et al., 1990). Based on a U–Pb zircon age, the formation of the ophiolite was dated to 443 ± 3 Ma (Pedersen et al., 1991). Texturally controlled in-situ U–Pb analysis of titanite using laser ablation-multicollector-ICMPS yielded an age of 442 ± 13 Ma interpreted to date ocean floor alteration of the ophiolite complex (Fliegel et al., 2011).

2.2. The Solund basin

Alluvial fan conglomerates and minor amounts of sandstones mainly compose the sediments of the Solund basin, organized in up to 100 meter-thick strata (Nilsen, 1968; Indrevær and Steel, 1975). Nilsen (1968) reported thirty distinct pebble lithologies in Solund basin of sedimentary, igneous and metamorphic origins. Sedimentary clasts consist of greywackes and siltstones, igneous clasts of granites, felsic rocks, diorites, gabbros, basalts, quartz aggregates and ultramafic rocks and metamorphic clasts of quartzites, micaschists, chlorite schists and gneisses. The distribution of these pebbles is complex and could reflect the adjacent basement geology (Nilsen, 1968). In the west and north, the conglomerate rests unconformably upon the Solund-Stavfjord ophiolite complex and associated metasedimentary rocks (Furnes et al., 1990; Fig. 1c). The Solund-Stavfjord ophiolite is composed of pillow lavas, pillow breccias, a sheeted dyke complex, gabbros and metahyaloclastites (Furnes, 1974) and is the closest onshore occurrence of non-redeposited basalts near the Solund basin (Fig. 1c). Peridotites cropping out on islands to the NW of the basin may be part of the ophiolite and a source for the peridotite clast within the basin (Beinlich et al., 2010). This ophiolite is probably a part of the ocean-floor of the Iapetus ocean and formed in a back-arc basin (Gale and Roberts, 1974). The sediments filling the Solund basin were mainly transported towards the northwest (Nilsen, 1968). The preserved stratigraphic thickness of the Solund basin is 6–7 km (Indrevær and Steel, 1975) and its onshore surface area is ~160 km^2.

Numerous veins transect the sediments of the Solund basin (Svensen et al., 2001). Svensen et al. (2001) found, based on fluid inclusions in these veins, that the sediments were buried to 12–14 km and the temperatures reached 230–320 °C.

2.3. Abundance and characterization of basaltic clasts

Nilsen (1968) reported on the basaltic clasts in the Solund basin and estimated that the percentage of basaltic clasts across the islands ranges from more than 30% on Ytre Solund to less than 1% in the east (Fig. 1e). The average percentage of basaltic clasts in the entire Solund basin is approximately 9% (Fig. 1e). For a sedimentary thickness of 6 km and assuming that the percentage of basalt does not change vertically, the total volume of basalt in this basin is thus close to 90 km^3. Basaltic clasts were sampled during two field trips at localities shown on Fig. 1c. Beinlich et al. (2010) noted that the red jasper-like clasts described by Nilsen (1968) are strongly altered peridotites. At proximity from these ultamafic clasts, basaltic clasts are also altered with reddened zoned colored by hematite (Fig. 2a). The reddened zones are paralleling the outline of the clasts. In a few cases the zones terminate towards the rims of the clasts suggesting a fragmentation of the clasts after their formation. Locally we find that the reddened zones developed around indentation points between two clasts, suggesting that the reddened zones formed during the compaction of the sediment. Generally, the clasts of the conglomerates range from 2 cm to 30 cm in diameter but boulders up to 1 m across occur. Clasts are generally smaller and strongly cemented with the matrix in the west whereas they are bigger and less cemented with the matrix in the east. Conglomerate rock properties similarly show a regional trend, reflected in the type of fracturing in response to blasting. In the west the conglomerate typically breaks along a planar surface whereas, in the east, the cleavage surfaces curve around the clasts. This difference in the behavior may indicate a deeper burial and a stronger compaction in the west compared to the eastern part.

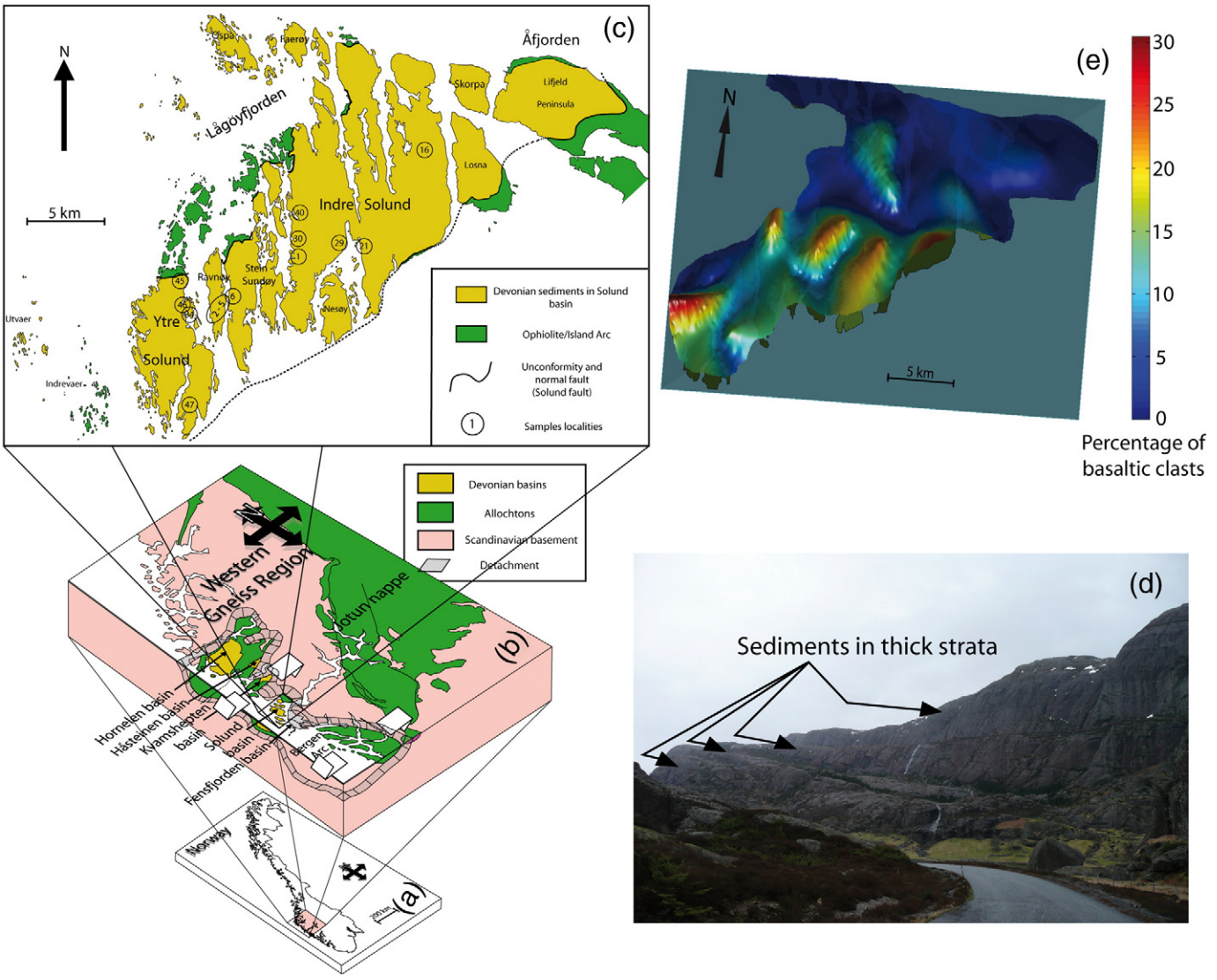

Fig. 1. Blow up diagram from Norway (a) to Solund basin (c) showing the detachment separating Devonian basins from the Western Gneiss Region (b). (c): Geological map of the Solund basin after Nilsen (1968) with sampling localities. Simplified geological map of Western Norway after Labrousse et al. (2004), Hacker et al. (2003) and Torgeir Andersen (oral communication). (d): Pictures of the folded strata of the Solund basin, locality 40. (e) Distribution of basaltic clasts on the Solund islands after Nilsen (1968). The third dimension is the proportional abundance of basaltic clasts. Note the increase of basaltic material from northeast to southwest in the basin. The average amount of basalts is 9 vol.% and their estimated volume amounts to 90 km^3.

3. Methods

3.1. Analytical methods

3.1.1. Whole rock composition

We sliced a total of fifteen samples with a diamond saw, separated the alteration zones from the other zones (see Section 4. for a description of the alteration zones) and crushed them in a steel mill. In samples where the alteration zones were too small to be separated, we determined an average chemistry.

We performed analyses of major and selected trace elements (Rb, Sr, Y, Zr, Nb, V, Cr, Co, Ni, Cu, Zn and Ba) of a total of 34 alteration zones. We measured loss on ignition (LOI) by weighing before and after heating the sample to 1000 °C, and correcting for the oxidation of FeO in the sample. Ignited material was mixed and fused with $Li_2B_4O_7$ in a mass ratio of 1:9 with a Philips Perl'x 3 instrument at the Institute of Geosciences, University of Oslo. The formed glass beads were analyzed by X-ray fluorescence with a Philips PW2400 spectrometer (Institute of Geosciences, University of Oslo). We used international standards of basalt and granite to calibrate the instrument. Accuracy was better than 1% for elements at concentrations above 1 wt.% and comprised in the 1–10% range at concentrations below 1 wt.%. The $Fe^{3+}/(Fe^{2+}+Fe^{3+})$ ratio was determined by titrimetric methods at the Department of Earth Sciences, Texas Tech, Lubbock, USA. The results are listed in Table 6.

3.1.2. EMP technique

We performed mineral analyses by wavelength-dispersive spectrometry (WDS), using a Cameca SX100 located at the Institute of Geosciences, Oslo University. The microprobe was operated with an accelerating voltage of 15 kV and a beam current of 15 nA. We acquired BSE images both by the microprobe and with a scanning electron microscope (JEOL JSM 6460LV) also located at the Institute of Geosciences, Oslo University. Results are listed in Tables 2, 3 and 4.

3.1.3. Micro-X-ray fluorescence technique

We generated maps of oxide distribution at the thin-section scale with micro-X-ray fluorescence. We used a micro-X-ray fluorescence

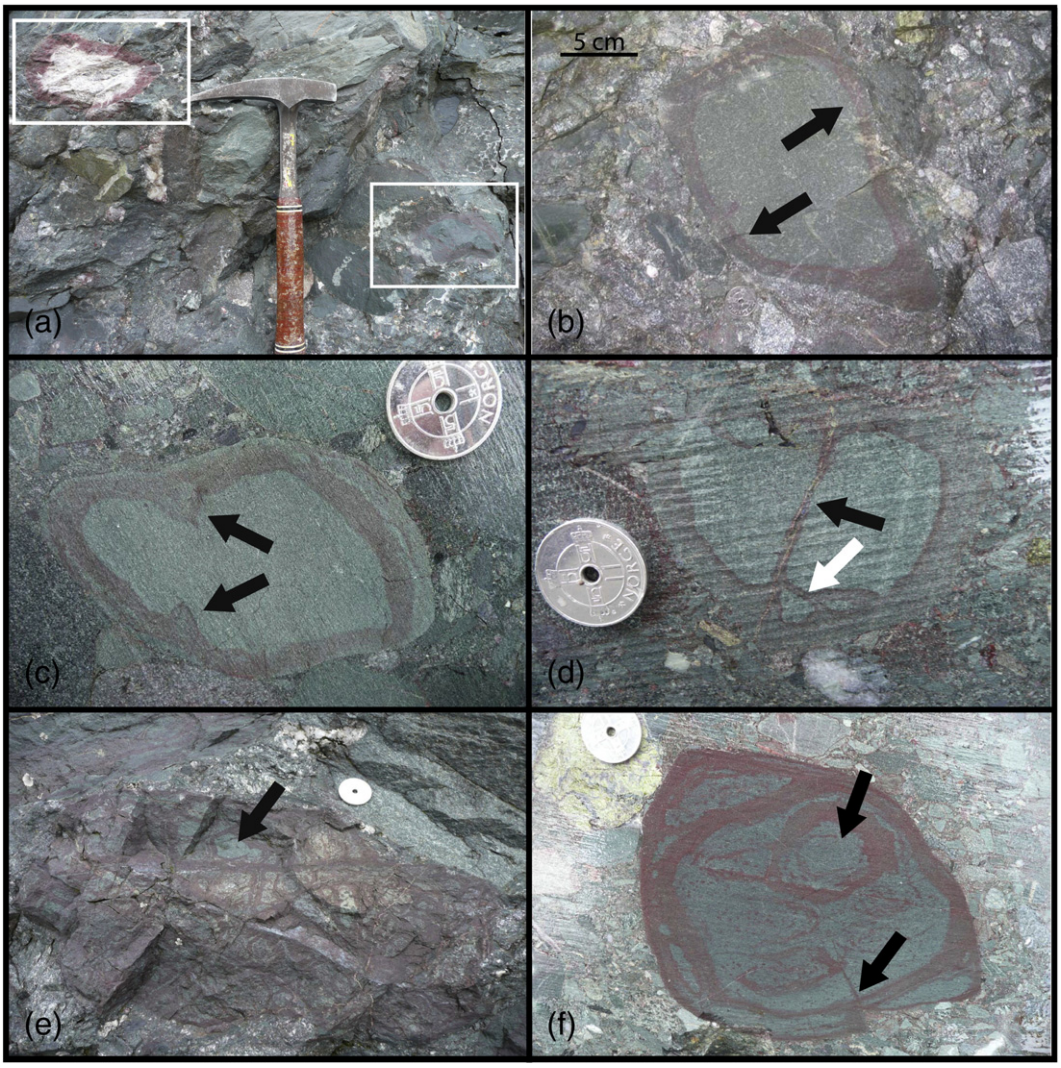

Fig. 2. Mosaic of pictures showing the different types of clasts observed in the field. Diameter of the coins: 2.1 cm. (a): field photo from locality 34 showing the close spatial relationship between altered peridotite (white square to the left) and basalt (white square to the right). (b): Clast with a concentrically arranged red zone following its surface (Type 1, locality 5). (c): Clast with two alteration zones following its surface (a red and a green zone). Note the presence of two perturbations propagating the alteration inwards (Type 2, locality 29). (d): Clast divided in two compartments by a fracture surrounded by red zones (Type 3, locality 29) (black arrow). Note the presence of two small inner green zones separated from the other inner green zones by red zones (white arrow). Streaks are artificial and were formed by the use of a saw. (e): Strongly divided clast where green material is surrounded by red alteration haloes (Type 3, locality 21). (f): Clasts showing complex patterns of alteration (Type 4, locality 29). Note the presence of several circular alteration haloes (arrow) which resembles Liesegang's rings and of a crack along which the conglomerate goes deeper into the clast (arrow, bottom of the clast).

spectrometer (Eagle III instrument located at the Institute of Earth Sciences, Grenoble University) with an accelerating voltage of 20 kV and a beam current of 300 μA. Spectra were acquired every 80 μm for 800 ms on a grid of 256 by 200 pixels corresponding to an area of approximately 2 by 1.5 cm. The software Visio32 was then used to extract from spectra the oxides concentrations in each pixel.

3.1.4. Sr isotopes

We analyzed variably altered domains of two different basaltic clasts for Rb–Sr isotope systematics. Rb and Sr concentrations were determined by isotope dilution using mixed ^{87}Rb–^{84}Sr spikes. Determinations of Sr isotope ratios were carried out on a Thermo-Finnigan Triton thermal ionization mass spectrometer at GFZ Potsdam, operated in dynamic multicollection mode. The value obtained for $^{87}Sr/^{86}Sr$ for the NBS standard SRM 987 was 0.710253 ± 0.000005 ($n = 9$). Rb isotopic compositions were determined using either a Thermo-Finnigan Neptune multicollector ICP-MS at GFZ Potsdam, or the Triton TIMS instrument. Accuracy of $^{87}Rb/^{86}Sr$ ratios is estimated as better than 1.5%. Total procedural blanks were consistently below 0.15 ng for both Rb and Sr. Blank-to-sample ratios were consistently very low, and no blank correction was applied. Results are listed in Table 8.

3.2. Imaging the alteration

We used 3D-images and mapping of cracks to investigate the relationship between alteration and deformation. We produced three dimensional images of the boulders as follows. We cut the boulder in parallel slices having a thickness ranging from 0.4 to 1.1 cm and we scanned the surface. Then, we oriented the slices in the same frame of reference and we drew the boundaries between different zones on each scan. Finally, we made a linear interpolation between the drawn boundaries to generate the three dimensional images.

We also mapped a dense network of cracks at the thin-section scale as follows. First, we acquired a high-definition scan (600 dpi) of the thin-section to map the main cracks. Then, we used pictures taken with a microscope to map smaller cracks. Finally, we verified the arrangement of the cracks by directly using the microscope.

4. Results

4.1. Types of basaltic clasts

Although gradual in their characteristics, the basaltic clasts were, for convenience of descriptions and data handling, divided into four structural types which are interpreted to represent an alteration-related evolutionary sequence (Fig. 2). The first group (Type 1) consists of boulders with a green core surrounded by hematite reddened 1–3 cm thick rims (Fig. 2b). In the second group (Type 2) the red zone makes excursions into the central part of the boulder and an outermost green zone is locally developed. The perturbations of the red zones occur along fractures, mineral-filled cracks, and microshear zones (Fig. 2c and d and Fig. 3). As can be seen from Figs. 2c and 3a and b, the fractures may penetrate deeper into the clasts than the red zones. Clasts of the third group (Type 3) show several compartments composed of a green core surrounded by red zones (Figs. 2d and e and 3c and d). Clasts of Type 4 display complex arrangements of green and red colored patches with circular and elliptical forms (Fig. 2f) with an outermost green zone. When multiple red zones occur, they are separated by thin green zones.

4.2. Structural evolution of the basaltic clasts

4.2.1. Relationship between alteration and deformation features

Table 1 lists the different kinds of deformation features that occur in the four types of clasts and the minerals that form in connection to the deformation structures. Table 1 shows that while the least altered clasts (Type 1) only display local hematite filled micro-cracks with a few major cracks perpendicular to the red zone, the more altered samples display dense networks of hematite micro-cracks (Fig. 4a, b and c), localized shear zones (Fig. 4d) and large veins opened and filled progressively. Typical grain size of the matrix correlates with the degree of alteration with very small grains in the most altered samples (Fig. 4a). Some of the Type 4 clasts have developed a penetrative banding defined by alternating green and red bands (Fig. 2f).

4.2.2. Development of compartments

Boulder SOL30-08I2 (Fig. 3c and d) belongs to Type 3 clasts and displays a complex pattern of red zones. An outer red zone surrounds the clast and extends ~2 cm from the edge inwards. A major fracture transects the boulder with two red zones developed parallel to this crack. This divides the boulder into two parts. These parts which are surrounded by red and outer green zones formed from fractures or from the boulder boundaries are called compartments. A second major fracture extends almost perpendicular out from this major crack and terminates inside the boulder (Fig. 3c and d). We interpret this as a frozen stage in the development of compartments and we suggest that the clast evolves through a sequential compartmentation during which few compartments are progressively divided into several other compartments. Fig. 3c and d also shows a crack that joins the surface of the boulder at nearly right angle. Dark green to red zones surround this fracture that divides the sample into two compartments.

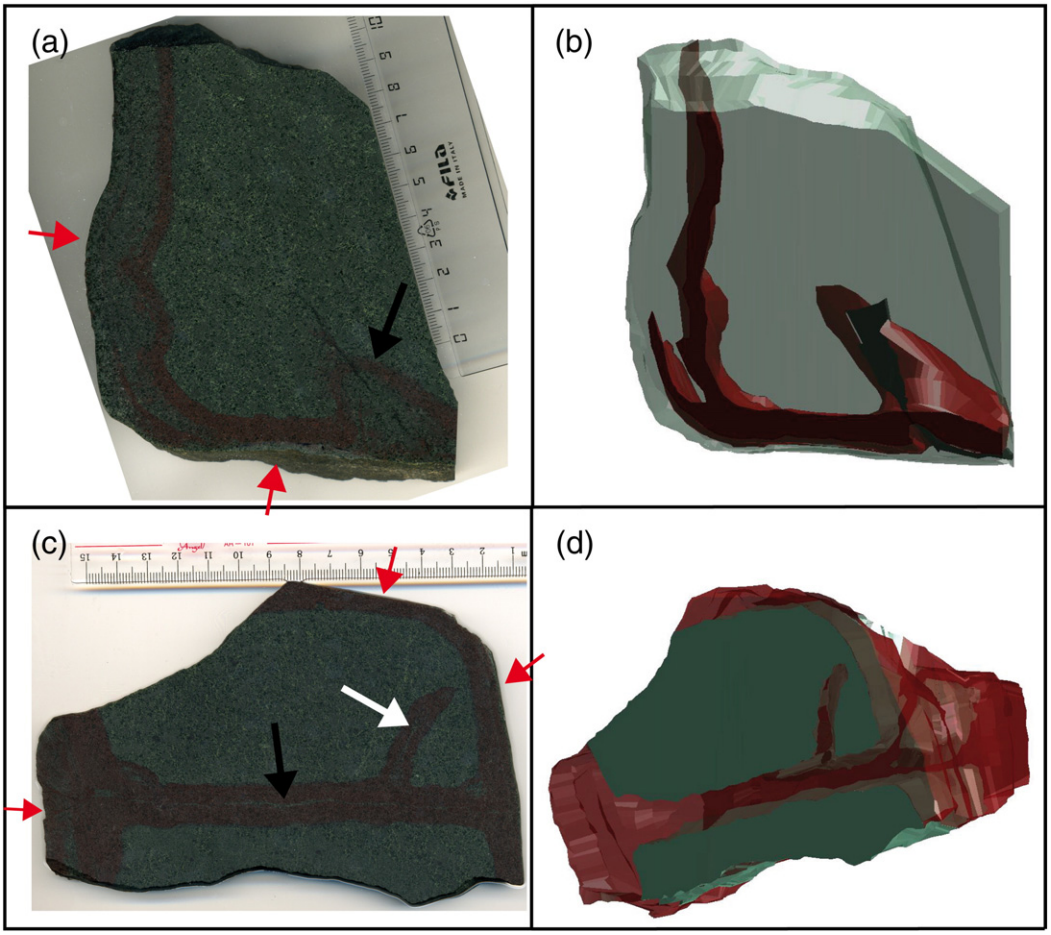

Fig. 3. Scans and 3D images of two samples. The surfaces of the boulders are indicated with red arrows. (a) and (b): Sample SOL43-04 (Type 2). The boulder displays two alteration zones (a red and a green one). Note that the inner contour of the red zone is sharp and the outer more diffuse. An oblique perturbation of the alteration zones (arrow on (a)) occurs close to a sharp corner of the boulder. It occurs symmetrically to a crack that goes deeper into the boulder. (c) and (d): Sample SOL30-08I2 (Type 3). The boulder is also surrounded by a red alteration zone. The boulder is divided into two compartments by a main crack and two red zones parallel to this crack (black arrow). A smaller crack joins this zone at nearly right angle (white arrow). The other side of this boulder shows numerous compartments separated by red zones and cracks.

Table 1
Deformation features in the samples.

Sample no.	Boulder type	Micro-cracks	Main cracks		Foliation
			Type A	Type B	
SOL40-04	1	x (f)			
SOL37-04	1	x (f)	x (ep, cal)		
SOL30-08C	2	x (d)			x
SOL43-04	2	x	x (ep, chl, hem)	x (qtz, Kfs, cal)	
SOL30-08B	3	x	x (ep, chl, hem, cal)		
SOL29-04	3	x (d)	x (ep, chl)	x (qtz, cal)	x
SOL30-08I2	3	x	x (ep, chl, hem)		
SOL30-08J	3	x (d)	x (ep, chl, hem, cal, qtz)	x (chl, Kfs, hem)	
SOL34-04	4	x (d)		x (qtz, cal)	
SOL30-08N1	4	x (d)	x (chl)		x

f: few micro-cracks.
d: dense network of micro-cracks.
See text for the definition of the boulder types.
Mineral abbreviations after Kretz (1983).

4.2.3. Distribution of micro-cracks

We mapped the micro-cracks of a thin-section of the most altered sample (SOL30-08J; Fig. 5). This thin-section shows a main central crack surrounded by a green zone which is separated from two green cores by red zones where a dense network of micro-cracks is observed. This main crack is developed as a shear zone. The micro-cracks are typically filled by hematite while the main cracks are filled by well-crystallized K-feldspar, hematite and/or chlorite. This particular filling of the main cracks suggests that these cracks are important transport channels of fluids and matter. Smaller fractures joining older fractures are also observed.

We determined statistical properties of the cracks of this thin-section (Fig. 5c and d) using the methodology described in Iyer et al. (2008). Two peaks are observable for the angles of junction of the cracks at 90° and slightly smaller than 180° (Fig. 5c). This suggests the predominance of T-junctions in this sample where a crack typically joins another crack at right angle and stops at its contact. Bohn et al. (2005a and 2005b) showed that T-shaped junctions are characteristic of sequential formation of different fracture generations. The mapped network appears thus to be composed of a succession of generations of fractures that we distinguished using the method of Bohn et al. (2005a, 2005b; Fig. 5b). The micro-cracks display two main orientations: odd generations parallel and even generations perpendicular to the main crack (Fig. 5d). This pattern also suggests a sequential formation of the cracks that develop at right angle to the cracks of older generations. Moreover, a more advanced stage of alteration (an amphibole-enriched green alteration zone, see Section 4.2.5.) is observed close to the main crack. This is in agreement with an evolution of the microfracturing starting from this main crack since, if this crack is the oldest one and propagated the alteration, the regions surrounding it will be more altered than the other regions. In the same way, cracks are hierarchically organized in sample SOL30-08J (Fig. 4a and b) where they display different fillings with epidote and chlorite in the older cracks and K-feldspar in the younger cracks. This could be related to a change in the fluid composition over time allowing us to distinguish between the older and the younger generations of cracks. This organization of the cracks suggests a progressive densification of the crack network.

4.2.4. Oblique cracks

In addition to micro-cracks which meet at right angles, sample SOL30-08J also contains faults that make an angle close to 45° with the main crack (Figs. 4a and b and 5b). These faults mainly developed in the red zones and they stop at the boundary of the red zone. They displace the micro-crack system indicating that they developed later. Displacement can be seen where oblique cracks are crossing older cracks. One of these cracks (Fig. 4b) divides the rock in two compartments by alteration zones. This suggests that these oblique cracks were formed and active during the alteration process.

4.2.5. Replacement of the red zones

We observed that another green or brown zone can separate the red zones from the boundary of the boulder and from the main fractures (Figs. 2, 3, 4 and 5). We often observed patches of red material which display diffuse boundaries in these green zones at proximity of the main cracks (Fig. 6). Moreover, a network of cracks which is spatially linked to the network of cracks observed in the red zones can cross these green zones (Fig. 5a). These observations suggest that these green zones around the main cracks represent an advanced stage of alteration which has replaced the red zones by dissolving or transporting hematite and locally leaving some remnant red patches.

4.2.6. Liesegang's rings

An alternation of hematite-rich and hematite-poor zones sometimes makes up the patches of red material (Fig. 6b). This feature is also observed at a larger scale, in the boulders of Type 4 (Fig. 2f) where concentric precipitation bands of hematite can be found. This organization of the red zones looks like Liesegang's rings (Liesegang, 1913, 1915) which are chemical patterns commonly observed when periodic precipitation occurs in reaction–diffusion systems.

This phenomenon is not well understood even though several theories were proposed to explain the formation of such patterns. The supersaturation theory (Ostwald, 1925) is the first and generally accepted theory to explain this phenomenon. In this theory, the nucleation and growth in a supersaturated fluid results in the depletion of reactants in the neighborhood. The repetition of this localized precipitation temporally and spatially leads to formation of zones where

Fig. 4. Structural and chemical changes in the most altered sample (SOL30-08J). (a): Scan of the thin-section with its interpretation (b) showing cracks (black) dividing the space in several compartments. These compartments are separated from the cracks by intensively fractured red zones (red) and amphibole-enriched green zones (light green). Some fractures are oblique and generate a displacement (red). One of these oblique cracks must have been formed during the alteration process since alteration zones are formed along it (white arrow). (c): BSE image from the red zone showing cracks filled by hematite. (d): BSE image showing a pull-apart structure along a shear zone. The arrows give the displacement along this shear zone. (e–j): Chemical maps on (a). (e): SiO_2 map. Note the decrease in the altered zones. (f): Fe_2O_3 map. Note the higher concentration in the red zones. (g): MgO map. Note the high concentration in the altered zones. (h): MnO map. Note the similarities of distribution with the Mg map. (i): CaO map. Note that CaO is highly concentrated along a vertical crack and slightly diffuses from it. (j): K_2O map. Note that K_2O is only highly concentrated in some cracks. Scale is from 0, the minimum measured concentration, to 1, the maximum measured concentration. The EDX semiquantification gives minimum and maximum values in wt.% of, respectively, 19.4 and 74.3 for SiO_2, 1.3 and 47.2 for Fe_2O_3, 0 and 33.6 for MgO, 0 and 0.5 for MnO, 0.1 and 18.9 for CaO, and 0 and 11.9 for K_2O. These concentrations are overestimated because volatiles cannot be measured with this technique.

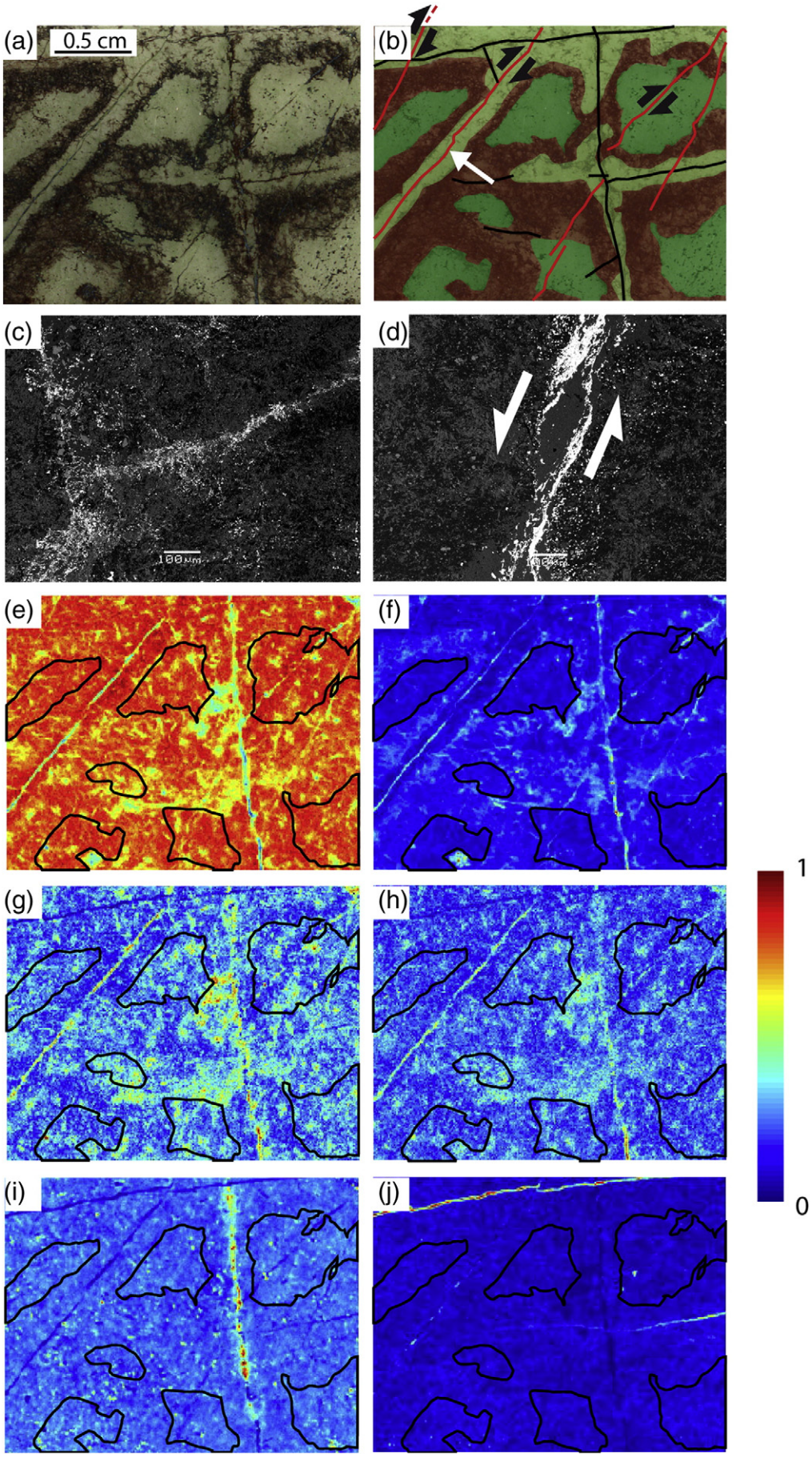
(a)
0.5 cm
(b)
(c)
(d)
(e)
(f)
(g)
(h)
(i)
(j)
1
0

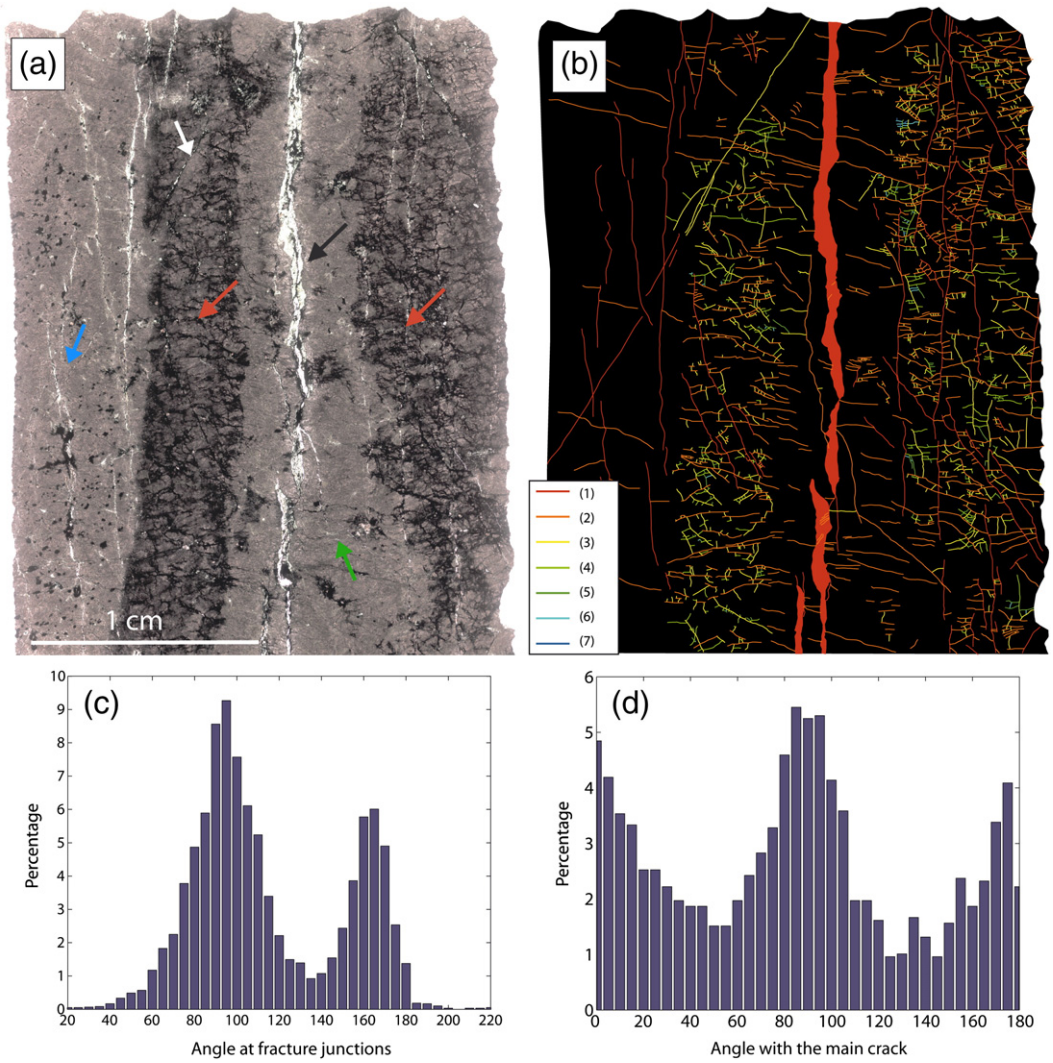

Fig. 5. Statistical study of one of the thin-sections of the most altered sample (SOL30-08J). (a): Scan of the thin-section showing a main crack filled by K-feldspar and chlorite (black arrow) surrounded by a green part (green arrow) and two red zones (red arrows) which separate it from the least altered part (blue arrow). Note the presence of oblique cracks which may have generated a displacement (white arrow). (b): Mapping of the different cracks of the thin-section. Different generations of micro-cracks mainly filled by hematite are distinguished with different colors (from the first generation (1) to the last one (7)). (c) and (d): Statistical properties of the mapped cracks. (c): Distribution of the angles at fracture junctions. Two peaks are observable at 90° and near 180° suggesting the predominance of T-junctions (two angles at 90° and a maximum angle at 180°). (d): Distribution of the orientation of the fractures showing the presence of two main orientations: parallel and perpendicular to the main crack. This suggests a propagation of the cracks from the main fracture.

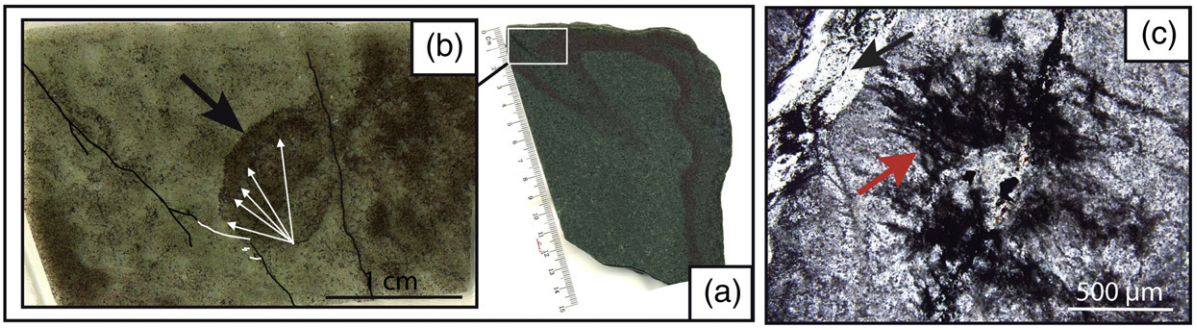

Fig. 6. Images of remnant red patches within green alteration zones. (a): Scan of sample SOL43-04 showing a perturbation with a crack followed by a red and a green alteration zones. (b): Scan of a thin-section providing a zoom in the green alteration zone. Note the presence of a red zone with a spheroidal form (black arrow) which is interpreted as a remnant zone. Note also the presence of bands with more hematite in this zone (white arrows) which resemble to Liesegang's structures. Main cracks are drawn in black for those that have a filling of hematite, epidote and chlorite and in white for those having a filling of K-feldspar, quartz and calcite. These cracks may have an important role in the formation of the patch by transporting fluid involved in the dissolution or in the transport of hematite. (c): Microscope picture of a remnant hematite patch in the green altered zone of sample SOL30-08J (red arrow). This patch is located close to a main fracture (black arrow).

precipitation has occurred separated by zones where precipitation has not occurred. Rings or bands will be formed depending on the geometry of the system. Formation of Liesegang's rings has been observed in many geological settings involving in particular hematite (Ohkawa et al., 2000) and products of alteration of basalts (Horváth et al., 2000).

4.3. Relationship between deformation and chemical changes

We investigated local chemistry through chemical maps acquired on six thin-sections. Results from sample SOL30-08J (Fig. 4) illustrate that the red zones reflect a redistribution of oxides (SiO_2, Fe_2O_3, MgO, MnO, CaO and K_2O) and that this redistribution relates to fracturing of the rock. Maps across the rim of the clasts (not shown) illustrate that chemical changes also propagate inwards from these boundaries with the surrounding environment. The highest concentrations of K_2O and CaO are measured in cracks related to the alteration zones, while TiO_2 sometimes concentrates in cracks which are not visible as a color change and may cross-cut the cracks that cause reddening. Fe_2O_3 strongly increases in the cracks and in the red zones. MgO and MnO behave in the same way by reaching their highest concentration in the alteration zones of the clasts even though their high concentration in these zones is not systematic. Generally, alteration zones are depleted in SiO_2 and in Al_2O_3. Conversely, the inner parts of the clasts display comparatively high concentrations in SiO_2 and Al_2O_3 and relative low concentrations in Fe_2O_3 and MnO.

4.4. Petrography and mineral chemistry

4.4.1. Primary magmatic mineralogy

The presence of clinopyroxene, plagioclase, chromite and hastingsite characterizes the least altered samples (Type 1 clasts; Table 2). These minerals are not observed in the more altered samples. Two textural varieties have been encountered: sample SOL29-04 contains plagioclase and clinopyroxene microliths in a matrix of spherulites which we interpret to be devitrified glass. Another textural variety displays a porphyritic texture, without spherulites. Clinopyroxenes are without inclusions and range in composition from diopside to augite (Table 2). They are zoned and show a range in MgO (16–11.5 wt.%) and FeO_{tot} (8.5–15 wt.%) resulting in Mg/(Mg + Fe) (XMg) ratio between 0.8 and 0.62. A comparison of the composition of these clinopyroxenes with clinopyroxene of known origin shows that they plot in the field of tholeiitic and alkaline basalt pyroxenes as defined by Schweitzer et al. (1979). Furnes et al. (1990) reported on the presence of tholeiitic and alkaline rocks in the adjacent Solund Stavfjord Ophiolite Complex (SSOC) which supports our hypothesis that the SSOC is the source rocks for the studied clasts. Consequently, the composition and the texture of these clinopyroxenes are in accordance with a magmatic origin and the zonation from Mg rich cores towards Fe-richer rims reflects a primary magmatic evolution.

Amphibole with a composition of hastingsite is present in sample SOL34-04 (Table 2). Hastingsite is a high temperature amphibole (Thomas, 1982) and therefore most likely of magmatic origin. Fe–Ti oxides are present in the least altered samples and are regarded as primary magmatic phases, just like more rare grains of chromite. EMP analyses of the Fe–Ti oxides (Table 3) give low totals which may suggest that part of the iron is present as Fe_2O_3 and that these grains are mixtures between ilmenite and titanohematite or pseudobrookite (solid solutions having for formula $Fe_{2-x}Ti_xO_3$ and $Fe_{1+x}Ti_{2-x}O_5$, respectively). It is unclear whether the oxidation of pure ilmenite formed the analyzed Fe–Ti oxide, or whether it represents a primary magmatic phase.

4.4.2. Formation of secondary minerals

Even in the least altered clasts the primary minerals show signs of alteration and formation of secondary minerals (Tables 2, 3 and 4). Epidote, chlorite, albite, titanite, secondary amphibole and hematite

Table 2
Composition of clinopyroxene and amphibole.

Clinopyroxene						Amphibole								
Sample	SOL40-04	SOL40-04	SOL40-04	SOL40-04	SOL40-04		SOL29-04	SOL29-04	SOL34-04	SOL34-04	SOL34-04	SOL34-04	SOL37-04	SOL40-04
Zone	R	I	R	I	R		R	R	R	I/Core	I/Core	I	I/Rim	R
SiO_2	49.66	49.98	50.21	49.30	48.59	SiO_2	49.81	54.75	38.62	50.86	50.01	48.47	53.50	53.34
TiO_2	1.53	1.50	1.36	1.32	1.97	TiO_2	0.05	0.02	0.13	0.22	1.37	0.91	0.83	0.02
Al_2O_3	2.91	3.86	3.83	2.17	3.05	Al_2O_3	4.56	0.92	17.06	1.68	4.09	5.64	1.24	0.83
FeO	13.72	9.56	8.75	15.07	13.62	FeO	17.59	13.35	24.16	25.50	16.56	17.79	17.22	18.06
MnO	0.33	0.26	0.20	0.45	0.38	MnO	0.21	0.32	0.41	0.49	0.47	0.51	0.28	0.44
MgO	14.22	15.93	16.02	11.64	11.95	MgO	11.76	15.44	3.04	7.19	11.85	11.39	11.94	12.08
CaO	17.27	18.47	18.83	19.18	19.18	CaO	12.29	12.97	11.82	12.01	12.43	12.39	12.60	12.47
Na_2O	0.37	0.31	0.35	0.34	0.42	Na_2O	0.65	0.09	1.27	0.27	0.46	0.61	0.25	0.09
Cr_2O_3	0.03	0.16	0.16	0.00	0.00	K_2O	0.21	0.02	1.02	0.03	0.08	0.20	0.04	0.02
Total	100.04	100.05	99.70	99.48	99.18	Cr_2O_3	0.07	0.00	0.03	0.01	0.03	0.10	0.01	0.00
						Total	97.20	97.87	97.57	98.26	97.36	98.03	97.92	97.36
Structural formula based on 6(O) and 4 cations						Structural formula based on 23(O)								
Si	1.866	1.848	1.858	1.889	1.859	Si	7.405	7.885	6.002	7.747	7.375	7.171	7.855	7.901
Ti	0.043	0.042	0.038	0.038	0.057	Ti	0.005	0.002	0.015	0.025	0.152	0.101	0.091	0.002
Al	0.129	0.168	0.167	0.098	0.138	Al	0.799	0.155	3.124	0.301	0.711	0.984	0.215	0.145
Fe^{3+}	0.078	0.070	0.061	0.074	0.063	Fe^{3+}	0.236	0.043	0.311	0.146	0.349	0.337	0.000	0.060
Fe^{2+}	0.353	0.226	0.210	0.409	0.372	Fe^{2+}	1.924	1.560	2.794	3.086	1.654	1.827	2.115	2.170
Mn	0.010	0.008	0.006	0.015	0.012	Mn	0.026	0.039	0.054	0.064	0.059	0.064	0.035	0.055
Mg	0.796	0.878	0.884	0.665	0.681	Mg	2.607	3.314	0.705	1.632	2.606	2.513	2.613	2.668
Ca	0.695	0.732	0.746	0.787	0.786	Ca	1.958	2.002	1.968	1.960	1.963	1.965	1.982	1.979
Na	0.027	0.023	0.025	0.025	0.031	Na	0.187	0.026	0.383	0.079	0.132	0.175	0.071	0.027
Cr	0.001	0.005	0.005	0.000	0.000	K	0.040	0.004	0.203	0.007	0.015	0.038	0.008	0.003
XMg	0.693	0.796	0.808	0.619	0.647	Cr	0.008	0.000	0.004	0.001	0.003	0.012	0.001	0.000
						XMg	0.575	0.680	0.201	0.346	0.612	0.579	0.553	0.551

R: red zone.
I: inner part.
Core: core of the grain.
Rim: rim of the grain.

Table 3
Composition of ilmenite, titanite and iron oxides.

Sample	Ilmenite		Sample	Titanite			Iron oxides			
	SOL29-04	SOL40-04		SOL 29-04	SOL34-04	SOL43-04	SOL29-04	SOL40-04	SOL43-04	SOL43-04
SiO_2	0.08	0.07	SiO_2	30.83	31.12	30.18	0.62	0.18	0.05	0.04
TiO_2	45.68	51.11	TiO_2	36.72	38.01	37.36	1.03	0.01	0.97	0.41
Al_2O_3	0.00	0.00	Al_2O_3	1.97	1.36	1.34	0.1	0.03	0.03	0.05
FeO	45.86	42.71	Fe_2O_3	1.75	1.16	2.51	96.68	100.88	98.01	99.26
MnO	4.23	1.87	MnO	0.04	0.05	0.05	0.06	0	0.02	0.08
MgO	0.02	0.02	MgO	0.10	0.00	0.00	0.04	0.02	0	0
CaO	0.21	0.43	CaO	28.53	28.35	28.48	0.15	0.06	0.08	0.02
Total	96.12	96.23	Total	99.93	100.06	99.91	98.68	101.18	99.16	99.84
Structural formula based on 3(O)			Structural formula based on 5(O)				Structural formula based on 3(O)			
Si	0.000	0.002	Si	1.011	1.016	0.997	0.018	0.005	0.001	0.001
Ti	0.928	1.004	Ti	0.905	0.934	0.928	0.023	0.000	0.022	0.009
Al	0.000	0.000	Al	0.076	0.052	0.052	0.004	0.001	0.001	0.002
Fe^{2+}	0.831	0.934	Fe^{3+}	0.043	0.029	0.063	1.934	1.989	1.964	1.983
Fe^{3+}	0.205	0.000	Mn	0.001	0.001	0.001	0.001	0.000	0.000	0.002
Mn	0.097	0.041	Mg	0.005	0.000	0.000	0.002	0.001	0.000	0.000
Mg	0.001	0.001	Ca	1.002	0.992	1.008	0.005	0.002	0.003	0.000
Ca	0.006	0.01								

are observed in all the samples while quartz, calcite, K-feldspar, plagioclase and muscovite were found in some of the thin-sections. Minor amounts of chalcopyrite, zircon and apatite are also present.

The primary clinopyroxenes and amphiboles are variably altered to fine grained chlorite, the alteration starting along grain boundaries and along cracks transecting the grains (Fig. 7a). Chlorite also occurs as a matrix mineral without clear connections to clinopyroxene and amphibole, and is a characteristic phase in the veins transecting the samples. Variations in the composition of the chlorite are observed but are difficult to link to any alteration zone or zonation. An unexplained zonation in the content in Cr_2O_3 may be observed with more than 1 wt.% of Cr_2O_3 content in the core of the chlorite. Chlorite ranges from a composition of clinochlore–daphnite to a solid solution between clinochlore–daphnite and amesite (Table 4). The chlorite XMg ratio is mainly close to 0.65 but some grains display a low XMg ratio of 0.55. Well-crystallized chlorites are also observed in many cracks but their composition is not significantly different from the chlorites of the matrix. We calculate the replacement of clinopyroxene by chlorite, assuming constant volume according to Gresens (1967) as follows (see Table 5):

$$100\ \text{g Cpx} + 14.3\ \text{g } Al_2O_3 + 10.1\ \text{g FeO} + 10.3\ \text{g } H_2O \rightarrow 89\ \text{g Chl} + 25.6\ \text{g } SiO_2 + 1.5\ \text{g } TiO_2 + 1\ \text{g MgO} + 17.6\ \text{g CaO}. \quad (1)$$

This reaction produces CaO and SiO_2 whereas it consumes FeO, Al_2O_3 and water at constant volume. Sericite and epidote + albite replace plagioclase.

The Fe–Ti phase occurs in all the zones but not in the most altered samples where a high modal percentage of titanite (>5%) is found. Titanite replaces the Fe–Ti oxides, which contain a comparatively high content of MnO (1–4 wt.%) along veins transecting the grains and at the boundary of the grains (Fig. 7b). This reaction can be balanced according to Gresens (1967) as follows, assuming constant volume and using the analyses of Table 3:

$$100\ \text{g Fe}-\text{Ti oxide} + 22.5\ \text{g } SiO_2 + 1\ \text{g } Al_2O_3 + 21\ \text{g CaO} \rightarrow 75.5\ \text{g Ttn} + 24.4\ \text{g } TiO_2 + 38.4\ \text{g FeO} + 5.2\ \text{g MnO}. \quad (2)$$

This reaction consumes mainly SiO_2 and CaO and releases TiO_2, FeO and MnO. Titanite sometimes displays worm like tubular textures which were studied in detail by Fliegel et al. (2011). The origin of these textures is unclear and could be biogenic.

4.4.3. The red zones

The presence of aggregates of quartz and hematite (Fig. 7c) and/or of cracks filled by hematite (micro-cracks) characterizes the red zones. Experiments by Otake et al. (2010) have shown that hematite can be formed by a non-redox transformation of magnetite and it consequently remains unclear if hematite formation in our samples is associated with an oxidation reaction. Calcite, locally present in the unaltered part, has not been found in the red zones. Small amounts of chalcopyrite are typically present in the red zones.

4.4.4. The outermost green zone

Amphibole-group minerals make up a few modal percent in the unaltered zone and are more abundant in the outer green zones, where they replace chlorite (Fig. 7d) and also form separate grains without any relationship to chlorite. Amphibole is typically fibrous and strongly zoned with XMg ratio ranging from 0.35 (ferro-hornblende) in the core to 0.85 in the rim (actinolite) (Table 2). A similar zoning of amphibole was reported by Beinlich et al. (2010) for amphibole clasts adjacent to the peridotite clasts. Beinlich et al. (2010) argued that the Mg-rich rim formed from Mg released from the reacting peridotite. Two reactions for amphibole formation can be written as follows for sample SOL30-08I2 using analytical data (Table 2) for amphibole core (C) and rim (R) compositions, respectively:

$$100\ \text{g Chl} + 27.3\ \text{g } SiO_2 + 0.1\ \text{g } TiO_2 + 3.2\ \text{g FeO} + 13.4\ \text{g CaO} + 1\ \text{g } Na_2O + 0.4\ \text{g } K_2O \rightarrow 115.5\ \text{g Amp(C)} + 12.7\ \text{g } Al_2O_3 + 0.1\ \text{g MnO} + 8.2\ \text{g MgO} + 0.1\ \text{g } Cr_2O_3 + 8.8\ \text{g } H_2O. \quad (3)$$

$$100\ \text{g Chl} + 32.9\ \text{g } SiO_2 + 0.1\ \text{g MnO} + 12.6\ \text{g CaO} + 0.5\ \text{g } Na_2O + 0.6\ \text{g } K_2O \rightarrow 109\ \text{g Amp(R)} + 18\ \text{g } Al_2O_3 + 10.1\ \text{g FeO} + 0.3\ \text{g MgO} + 0.1\ \text{g } Cr_2O_3 + 9.6\ \text{g } H_2O. \quad (4)$$

The formation of amphibole from chlorite releases two different sets of chemical compounds depending on the composition of the formed amphibole. If the amphibole is rich in iron, the reaction releases a large amount of MgO in the system and consumes FeO_{tot} (3.2 g per 100 g of chlorite) whereas, if the amphibole is rich in magnesium, the reaction only produces small amounts of MgO and releases FeO_{tot} (10.1 g per 100 g of chlorite). This reaction is also Ca-consuming and Al-releasing.

Table 4
Composition of chlorite and epidote.

Chlorite														Epidote											
Sample	SOL29-04	SOL34-04	SOL34-04	SOL37-04	SOL40-04	SOL40-04	SOL43-04	SOL43-04	SOL43-04	SOL43-04	SOL43-04	SOL30-08I2	SOL30-08 J	Sample	SOL 29-04	SOL29-04	SOL34-04	SOL34-04	SOL37-04	SOL40-04	SOL40-04	SOL43-04	SOL43-04	SOL43-04	SOL30-08 J
Zone	R	I	I	I	R	I	I/Core	R/Core	I	O	R/Rim	R/Rim	I/Rim	Zone	R	R	R	R/Core	I	R	I	R	I/Core	R	I/Core
SiO_2	26.64	26.67	28.70	25.41	27.52	26.90	29.94	31.12	26.72	28.11	26.90	27.41	28.28	SiO_2	38.29	38.37	37.82	37.10	37.95	37.72	37.78	37.25	40.84	38.21	39.27
TiO_2	0.04	0.20	2.46	0.01	0.01	0.03	0.01	0.00	0.05	0.03	0.02	0.00	0.08	TiO_2	0.08	0.07	0.06	0.08	0.07	0.10	0.15	0.07	0.08	0.08	0.03
Al_2O_3	19.65	19.94	16.09	18.06	17.22	19.26	16.02	15.80	20.50	19.22	19.45	19.18	19.04	Al_2O_3	26.45	27.61	25.69	21.15	24.30	24.63	24.79	22.11	30.86	24.78	23.98
FeO	25.08	25.17	20.71	27.76	23.78	26.60	18.40	17.52	21.44	18.93	23.04	21.13	18.38	Fe_2O_3	8.94	7.60	10.47	16.35	11.66	11.17	10.98	14.69	2.45	11.69	10.32
MnO	0.54	0.66	0.57	0.39	0.46	0.63	0.54	0.38	0.81	0.47	0.57	0.57	0.48	MnO	0.09	0.12	0.23	0.17	0.11	0.06	0.28	0.12	0.14	0.14	0.14
MgO	15.36	15.70	16.21	13.47	17.43	14.76	21.04	22.00	17.94	20.40	16.77	19.18	20.72	MgO	0.00	0.01	0.01	0.00	0.01	0.00	0.01	0.00	0.16	0.00	1.16
CaO	0.09	0.20	2.47	0.12	0.08	0.05	0.22	0.15	0.05	0.07	0.13	0.21	0.07	CaO	24.05	24.14	23.69	23.35	23.97	24.17	23.39	23.36	23.19	23.95	22.97
Na_2O	0.03	0.01	0.05	0.03	0.02	0.06	0.08	0.01	0.01	0.02	0.07	0.00	0.00	Cr_2O_3	0.02	0.00	0.07	0.03	0.00	0.00	0.00	0.01	0.00	0.02	0.02
K_2O	0.01	0.01	0.14	0.01	0.00	0.01	0.09	0.03	0.01	0.08	0.02	0.01	0.00	Total	97.91	97.91	98.03	98.23	98.06	97.85	97.38	97.60	97.70	98.88	97.87
Cr_2O_3	0.04	0.00	0.05	0.02	0.05	0.21	1.00	0.53	0.00	0.04	0.00	0.24	0.02												
Total	87.48	88.55	87.44	85.29	86.58	88.50	87.35	87.53	87.51	87.36	86.97	87.93	87.07												
Structural formula based on 28(O)														Structural formula based on 12.5 (O)											
Si	5.626	5.567	5.982	5.621	5.840	5.662	6.119	6.280	5.534	5.743	5.655	5.644	5.776	Si	3.066	3.047	3.054	3.105	3.088	3.070	3.081	3.103	3.115	3.080	3.161
Ti	0.006	0.032	0.385	0.002	0.002	0.004	0.002	0.000	0.007	0.004	0.003	0.000	0.012	Ti	0.005	0.004	0.004	0.005	0.004	0.006	0.009	0.004	0.004	0.005	0.002
Al	4.891	4.906	3.952	4.709	4.307	4.778	3.860	3.757	5.004	4.628	4.820	4.654	4.584	Al	2.496	2.584	2.445	2.086	2.330	2.363	2.383	2.171	2.775	2.355	2.275
Fe^{3+}	0.000	0.000	0.000	0.000	0.000	0.000	0.000	0.000	0.000	0.000	0.000	0.000	0.000	Fe^{3+}	0.544	0.459	0.643	1.040	0.721	0.691	0.681	0.930	0.142	0.717	0.625
Fe^{2+}	4.429	4.394	3.609	5.136	4.221	4.683	3.145	2.956	3.714	3.233	4.050	3.639	3.139	Mn	0.006	0.008	0.016	0.012	0.007	0.004	0.019	0.009	0.009	0.010	0.009
Mn	0.096	0.116	0.100	0.074	0.083	0.112	0.094	0.064	0.142	0.081	0.102	0.100	0.082	Mg	0.000	0.002	0.001	0.000	0.002	0.000	0.001	0.000	0.018	0.000	0.139
Mg	4.836	4.886	5.036	4.441	5.516	4.630	6.412	6.620	5.540	6.213	5.255	5.887	6.308	Ca	2.063	2.054	2.050	2.094	2.090	2.108	2.044	2.085	1.896	2.069	1.982
Ca	0.021	0.045	0.550	0.028	0.019	0.011	0.048	0.032	0.011	0.015	0.029	0.046	0.016	Cr	0.001	0.000	0.004	0.002	0.000	0.000	0.000	0.001	0.000	0.001	0.001
Na	0.012	0.003	0.020	0.012	0.006	0.024	0.031	0.002	0.005	0.006	0.027	0.000	0.000												
K	0.001	0.002	0.037	0.004	0.001	0.003	0.024	0.009	0.001	0.022	0.006	0.002	0.000												
Cr	0.007	0.000	0.008	0.003	0.009	0.034	0.162	0.085	0.000	0.006	0.000	0.039	0.003												
XMg	0.522	0.527	0.583	0.464	0.567	0.497	0.671	0.691	0.599	0.658	0.565	0.618	0.668												

R: red zone.
I: inner part.
Core: core of the grain.
Rim: rim of the grain.

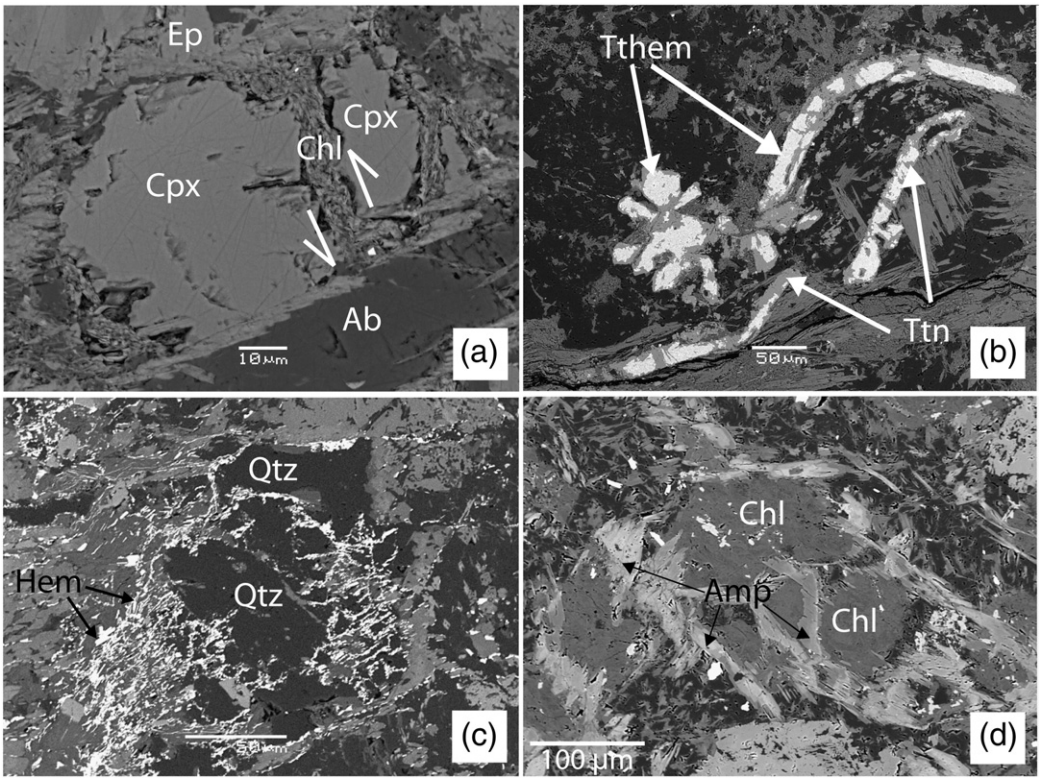

Fig. 7. BSE images showing the main mineralogical changes observed in the rock. Progressive disappearance of the altered phases towards the center and along transecting veins is generally observed. (a): Replacement of clinopyroxene by chlorite in the least altered sample (SOL40-04). Note a possible displacement along a transecting vein (arrows). (b): Replacement of titanohematite by titanite (sample 37-04). (c): Aggregate of quartz and hematite. Tiny grains of hematite (<5 µm) are typically aligned. (d): Replacement of chlorite by a zoned amphibole (sample SOL 43-04). The core of the amphiboles is Fe-rich and the rim is Mg-rich. Amp: amphibole; Tthem: titanohematite. Other mineral abbreviations after Kretz (1983).

Epidote is also one of the characteristic minerals in the altered basalts. Epidote typically displays a high Fe_2O_3 content mainly ranging from 11 to 15 wt.% even though epidote grains with low content in Fe_2O_3 were found (Table 4).

4.5. Whole-rock chemistry

4.5.1. Major elements

The samples are characterized by highly variable oxidation states as represented by $Fe^{3+}/(Fe^{3+}+Fe^{2+})$ ratios between 0.18 and 0.57 (Table 6), variable K_2O contents (0.1–1.9 wt.%) and a high volatile contents represented by LOI values — mostly between 3 and 5 and reaching ~10 wt.% in the most altered sample. We distinguish three groups of samples, based on major elements chemistry, and we associate these groups with the four types of clasts defined on a structural basis:

- Group P (primitive samples – Type 1 – Table 6) which comprises samples with a low $Fe^{3+}/(Fe^{3+}+Fe^{2+})$ ratio (0.27 ± 0.07 — values are given on average followed by their standard deviation, see Table 7) and a low K_2O content (0.22 ± 0.07 wt.%). The CaO content decreases or is constant from the inner part to the outer one (9.5 ± 0.4 wt.%). For sample SOL01-08, an increase in the oxidation state is observed in the red zones compared to the green core. MgO content varies from 5.4 to 6.5 wt.% in these boulders and loss on ignition (LOI) is low (3.0 ± 0.7 wt.%).
- Group A (altered samples – Type 2 – Table 6) comprises the majority of the samples. These samples are characterized by a higher

Table 5
Gresens analyses of mineral replacements assuming constant volume.

Sample	SOL40-04	SOL40-04		SOL43-04	SOL43-04		SOL30-08I2 Core	SOL30-08I2 Core		SOL30-08I2 Rim	SOL30-08I2 Rim	
	Cpx	Chl	G/L	Tthem	Tit	G/L	Chl	Amp	G/L	Chl	Amp	G/L
SiO_2	49.66	26.90	−25.6	0.08	30.18	22.5	27.50	47.47	27.3	27.50	55.64	32.9
TiO_2	1.53	0.03	−1.5	52.31	37.36	−24.4	0.09	0.14	0.1	0.09	0.11	0.0
Al_2O_3	2.91	19.26	14.3	0.04	1.34	1.0	19.52	5.90	−12.7	19.52	1.40	−18.0
FeO	13.72	26.60	10.1	40.1	2.26	−38.4	22.14	21.92	3.2	22.14	11.06	−10.1
MnO	0.33	0.63	0.2	5.09	0.05	−5.1	0.50	0.38	−0.1	0.50	0.52	0.1
MgO	14.22	14.76	−1.0	0.04	0.00	0.0	17.61	8.13	−8.2	17.61	15.94	−0.3
CaO	17.27	0.05	17.2	0.23	28.48	21.0	0.07	11.68	13.4	0.07	11.71	12.6
Na_2O	0.37	0.06	−0.3	0.03	0.00	0.0	0.00	0.83	1.0	0.00	0.43	0.5
K_2O	0.00	0.01	0.0	0	0.00	0.0	0.00	0.36	0.4	0.00	0.59	0.6
Cr_2O_3	0.03	0.21	0.2	0.01	0.00	0.0	0.13	0.05	−0.1	0.13	0.00	−0.1
H_2O	0.00	11.50	10.3	0	0.00	0.0	12.44	3.15	−8.8	12.44	2.59	−9.6
Density	3.30	2.95		4.75	3.55		2.90	3.35		2.90	3.15	

$Fe^{3+}/(Fe^{3+}+Fe^{2+})$ ratio (0.46 ± 0.07), enrichments in MgO (6.8 ± 0.7 wt.%), K_2O (0.86 ± 0.39 wt.%) and volatiles, approximated as LOI (3.4 ± 0.5 wt.%) and a depletion in CaO (7.9 ± 0.5 wt.%) relative to group P. Among the samples of this group, chemical variations are observed between the least and the most altered zones with MgO, K_2O and LOI increases and a CaO decrease. No systematic variation in the $Fe^{3+}/(Fe^{3+}+Fe^{2+})$ ratio is observed between the zones.

– Group MA, (the most altered samples – Types 3 and 4 – Table 6) which is composed of two extremely altered zones of boulders SOL30-08I2 and SOL30-08J, display the same features as the samples of group A but to a higher degree. Thus, we found very high values for MgO (up to 13.4 wt.% and 14.2 wt.%, respectively) and for LOI (from 3.5 to 9.6 wt.% respectively) and a low content in CaO (6.7 and 5.8 wt.%, respectively). These zones display also a strong decrease in SiO_2 content (39.7 wt.% and 37.6 wt.%, respectively) and high increases in MnO (up to 0.3 wt.% in both samples) and FeO (16.6 and 15.7 wt.%, respectively) contents. We also note that a totally brown sample (SOL30-08E) displays a high content in volatiles associated with a loss on ignition of 4.55 wt.%.

4.5.2. Trace elements

Sr content decreases from the least to the most altered zones through all the samples (Fig. 8). For instance, this content is reduced by half from the least to the most altered zone in the most altered sample (SOL30-08J). Low concentrations of Rb and Ba compared to the more altered clast types characterize type P clasts. This suggests that these elements, like K_2O, are introduced during the alteration. Almost all the samples display a reduction of Cr content with the degree of alteration. Except for the two most altered samples, the content in Co decreases from the least to the most altered zones of each boulder. Variation of Co content is decoupled from the variation of Ni content. Among the trace elements, Cu shows the strongest variations from 18 to 1096 ppm.

4.5.3. Comparison with basalts from the Solund-Stavfjord Ophiolite Complex

The Solund-Stavfjord Ophiolite Complex (Fig. 1) is the spatially closest potential source region for the basalt and peridotitic clasts in the Solund basin (Beinlich et al., 2010). So, it is likely that the basalts that were altered in the Solund basin originally had a composition close to those of the Solund-Stavjord Ophiolite Complex (SSOC). Compositions of basalts from the SSOC have been published by Furnes et al. (1982), Furnes et al. (1990), Ryttvad et al. (2000), Fonneland-Jørgensen et al. (2005) and Furnes et al. (2006). These papers give a total of 101 analyses (including sheeted flows, dykes and pillow lavas). We used these data to make a comparison between the basaltic clasts in the basin and the basalts of the SSOC (Table 7).

The contents in SiO_2, TiO_2, Al_2O_3, Na_2O, Y, Zr, V, Co, Ni and Zn are very similar in the two groups of basalts. Moreover, the plot of TiO_2 vs Zr (both regarded as immobile) places the samples of the ophiolite and of the basin on the same line (Fig. 9a). These similarities are in agreement with the assumption of an origin of the basaltic clasts of the Solund basin from the SSOC.

However, some clear compositional differences exist between the two groups of basalts. Altered basalts of the Solund basin contain more K_2O and less CaO than those of the SSOC (Fig. 9b and c). Samples from the basin seem to display also a higher content of volatile components, reflected in the loss on ignition data and they have markedly higher $Fe^{3+}/(Fe^{3+}+Fe^{2+})$ ratios.

For the trace elements, the main differences are observed in the Rb contents (Fig. 9b). The basalts of this study and those of the Solund-Stavfjord Ophiolite Complex display very different signatures with respect to Rb. Fig. 9b and c shows that Solund basin basalts of group P are compositionally closest to those of the SSOC. So, this group seems to be composed of primary basalts with a composition indicating that they underwent a less strong metasomatism than the other altered basalts.

4.5.3.1. Isocon diagrams — quantification of chemical changes.

To outline and visualize the chemical changes during the alteration, we generated an isocon diagram (Grant, 2005; Fig. 10). This kind of diagram allows us, by comparing an original rock to its altered equivalent, to quantify the loss and gain of elements and the change of volume that occur during alteration by assuming that a component is immobile.

We determined for each group an average composition with a standard deviation that we compared to an average composition of the basalts from the Solund-Stavfjord Ophiolite Complex (SSOC; Table 7 and Fig. 10). Compared to the SSOC, K_2O, Fe_2O_3, loss on ignition contents and Rb are higher and CaO and FeO contents are lower for the altered and most altered groups of the Solund basin. MgO is also higher in the most altered samples.

4.6. Sr isotopic constraints on alteration processes

In the altered basaltic clasts of the Solund basin, $^{87}Sr/^{86}Sr$ isotope ratios between 0.7081 and 0.7122 were measured (Table 8). Because textural observations of the alteration patterns suggest that alteration occurred within the Devonian Solund basin, we follow Beinlich et al. (2010) and regard a Middle Devonian age of 385 Ma, closely after conglomerate deposition, as the most likely time of intrabasinal alteration. The apparent $^{87}Sr/^{86}Sr$ ratios calculated for t = 385 Ma are nearly identical at 0.7072 for sample SOL43-04, and vary between 0.7073 and 0.7103 for different parts of sample SOL30-08 (Table 8). These isotopic ratios are considerably higher than those expected for Phanerozoic depleted-mantle derivatives (0.702–0.705, e.g., Zindler and Hart, 1986). They are also consistently higher than the isotopic ratios measured for basaltic rocks of the SSOC, which are generally at or below 0.705 (Furnes et al., 2000). The $^{87}Sr/^{86}Sr$ ratio at 385 Ma of our sample SOL30-08JG is, with 0.7103, also higher than that of Devonian ocean water which never exceeded a value of 0.7092 (Howarth and McArthur, 1997; McArthur et al., 2001). The Sr isotopic ratios of the here analyzed basaltic clasts are, however, distinctly lower than those of the ultramafic clasts of the Solund basin which have ratios all higher than 0.7124 at t = 385 Ma (Beinlich et al., 2010). This set of data suggests that a major overprint of the basaltic clasts occurred within the Solund basin, most likely by reaction with intrabasinal fluids. These fluids carried radiogenic Sr, most probably derived from old continental detritus within the basin, and had average $^{87}Sr/^{86}Sr$ ratios higher than 0.7124 (Beinlich et al., 2010). The isotopic ratios of our altered basaltic clasts are thus intermediate between the compositions of the SSOC basalt sources and the intrabasinal fluids. This means that there was strong but limited, alteration-related exchange of Sr (or, more generally, matter) with the intrabasinal fluids. This exchange nevertheless did not run to completion, since the Sr isotopic ratios of the basaltic clasts are still markedly lower than those of the ultramafic clasts of Beinlich et al. (2010) which acquired most of their Sr from the fluids and thus are good proxies for the Sr composition of the fluids. Such a limited exchange of Sr during intrabasinal alteration is in line with our textural observations which show that various stages of alteration are preserved and that also mineralogical relics of the precursor basaltic rocks are preserved. Our sample with the highest $^{87}Sr/^{86}Sr$ ratio at t = 385 Ma (0.7103 for sample SOL30-08JG) is also the sample which chemically departs most markedly from an average basaltic composition. It shows a whole rock composition pointing to a chlorite-dominated assemblage (Table 6) and thus most probably has the strongest metasomatic imprint of our sample set. This observation confirms that the basaltic clasts interacted with a basinal fluid carrying a very radiogenic Sr ($^{87}Sr/^{86}Sr$ higher than contemporaneous seawater) and that an increasingly intense metasomatic overprint of

Table 6
Major and trace element composition of samples sorted according to their degree of alteration.

Sample	SOL 01-08	SOL 01-08	SOL 02-08K	SOL 02-08K	SOL 29-04	SOL30-08N1**	SOL30-08N1**	SOL30-08N1*	SOL 30-08N2	SOL 30-08A**	SOL 30-08A*	SOL 30-08A*	SOL30-08B**	SOL30-08B	SOL30-08B	SOL30-08B*	SOL30-08C**
Alteration zone	R	I	R	I	M	R	R	I	M	R	I (1)	I (2)	R	Int	Int	I	R
Group	P	P	P	P	P	A	A	A	A	A	A	A	A	A	A	A	A
Locality	1	1	2	2	45	30	30	30	30	30	30	30	30	30	30	30	30
Major elements (wt.%)																	
SiO_2	48.60	47.36	47.52	47.69	48.08	48.03	47.45	48.36	47.39	49.08	48.82	49.30	48.02	48.21	48.10	47.78	47.98
TiO_2	3.11	2.87	3.18	3.17	2.14	2.56	2.64	2.59	2.58	2.74	2.87	2.85	2.31	2.32	2.37	2.33	2.36
Al_2O_3	13.17	12.49	12.51	12.52	14.61	12.90	13.27	13.05	13.05	13.32	13.12	13.25	13.36	13.48	13.48	13.48	13.09
Fe_2O_3T	14.66	15.87	16.15	15.39	12.36	14.42	14.91	14.20	14.23	14.52	15.31	15.10	13.16	13.72	13.90	13.83	12.83
Fe_2O_3	4.94	2.91	n.a.	3.97	3.81	6.94	7.60	6.72	6.39	7.99	8.75	8.66	5.70	6.21	6.10	6.12	5.18
FeO	8.75	11.66	n.a.	10.82	7.69	6.73	6.58	6.73	7.06	5.88	5.90	5.80	6.71	6.76	7.02	6.94	6.89
Fe^{3+}/Fe_{total}	0.34	0.18	n.a.	0.25	0.31	0.48	0.51	0.47	0.45	0.55	0.57	0.57	0.43	0.45	0.44	0.44	0.40
MnO	0.22	0.25	0.24	0.25	0.18	0.20	0.20	0.19	0.20	0.17	0.18	0.18	0.19	0.18	0.19	0.19	0.18
MgO	5.35	5.37	5.65	5.67	6.54	6.74	6.52	6.18	7.19	6.87	5.96	5.99	6.81	6.33	6.61	6.21	8.01
CaO	8.94	10.12	9.22	9.42	9.57	8.25	8.37	8.52	8.48	6.67	7.03	7.01	8.26	8.26	7.60	8.19	7.93
Na_2O	2.46	1.98	3.01	2.86	3.40	3.45	3.52	3.62	3.30	2.70	2.87	2.96	2.60	2.92	3.03	2.84	2.50
K_2O	0.28	0.26	0.18	0.13	0.27	0.62	0.59	0.59	0.49	0.59	0.58	0.53	0.98	1.09	1.05	1.04	1.62
P_2O_5	0.25	0.23	0.28	0.28	0.16	0.22	0.22	0.21	0.21	0.24	0.25	0.25	0.19	0.19	0.20	0.19	0.18
LOI	2.42	2.31	1.88	1.93	2.39	2.30	2.25	2.15	2.46	3.05	2.69	2.67	2.96	2.91	2.88	2.85	2.66
LOIc	3.39	3.60	1.88	3.13	3.24	3.05	2.98	2.90	3.24	3.70	3.34	3.31	3.70	3.66	3.66	3.62	3.42
SUM	99.46	99.09	99.82	99.30	99.71	99.68	99.93	99.66	99.58	99.95	99.68	100.11	98.85	99.61	99.40	98.93	99.35
Trace elements (ppm)																	
Rb	19	19	7	7	12	18	18	16	15	26	24	23	39	40	37	37	46
Sr	113	126	128	130	206	150	159	158	151	215	221	216	222	227	198	229	167
Y	71	64	69	69	49	57	57	56	57	63	64	65	52	53	54	54	52
Zr	211	192	233	233	143	180	185	181	182	197	195	208	161	160	163	161	161
Nb	5	4	4	5	4	4	4	5	4	5	5	4	4	3	2	4	4
V	518	468	504	497	376	403	431	430	411	408	439	430	375	382	390	403	367
Cr	96	99	109	114	435	130	134	160	183	279	305	271	231	226	229	369	207
Co	41	42	41	53	45	39	47	49	44	40	53	48	38	47	44	54	42
Ni	37	37	45	49	143	56	52	52	58	64	60	53	62	59	58	67	75
Cu	22	25	162	230	39	50	29	352	31	190	250	143	270	297	156	130	428
Zn	103	92	128	132	98	114	131	119	147	117	133	131	104	109	110	109	96
Ba	12	7	12	Trace	22	112	92	92	72	80	64	67	121	147	152	137	495

*: sample used to calculate a mean composition of the least altered zones for diagrams of Grant.
**: sample used to calculate a mean composition of the most altered zones for diagrams of Grant.
R: red zone.
I: inner part.
Int: intermediate zone between red zone and outer zone.
M: mix between red and green material (difficult to separate).
P, A: see text for definition.

Sample	SOL30-08C**	SOL30-08C*	SOL 30-08L	SOL 30-08H**	SOL 30-08H*	SOL 34-04	SOL43-04**	SOL43-04**	SOL43-04*	SOL30-08E**	SOL30-08I2**	SOL30-08I2**	SOL30-08I2*	SOL30-08I2*	SOL30-08J	SOL30-08J**	SOL30-08J**
Alteration zone	Int	I	M	R	I	M	O	R	I	Int	R(boundary)	R(inside)	I(1)	I(2)	G	M	M
Group	A	A	A	A	A	A	A	A	A	A	MA	MA	MA	MA	MA	MA	MA
Locality	30	30	30	30	30	46	30	30	30	30	30	30	30	30	30	30	30
Major elements (wt.%)																	
SiO_2	46.77	48.02	48.63	46.45	48.68	48.24	48.90	48.46	47.28	48.55	39.75	46.97	47.53	48.00	37.58	52.40	48.51
TiO_2	2.37	2.34	2.59	2.50	2.45	2.82	2.43	2.39	2.35	2.50	2.21	2.49	2.61	2.45	2.11	1.85	1.96
Al_2O_3	13.44	13.49	12.49	13.78	13.68	13.82	12.62	13.65	13.79	12.72	15.12	14.13	13.87	14.39	14.25	14.30	14.41
Fe_2O_3T	13.20	13.42	14.46	13.64	14.01	14.71	12.82	13.07	13.70	13.47	16.59	15.08	14.80	14.46	15.69	11.13	10.50
Fe_2O_3	5.61	6.71	6.56	6.26	7.15	4.24	4.50	5.99	n.a.	6.98	8.67	7.56	7.06	7.43	2.93	3.90	2.89
FeO	6.83	6.04	7.10	6.64	6.17	8.81	7.49	6.37	n.a.	5.84	7.13	6.76	6.92	6.32	11.48	6.51	6.85
Fe^{3+}/Fe_{total}	0.42	0.50	0.45	0.46	0.51	0.30	0.35	0.46	n.a.	0.52	0.52	0.50	0.48	0.51	0.19	0.35	0.28
MnO	0.19	0.16	0.19	0.18	0.17	0.29	0.20	0.20	0.22	0.17	0.30	0.19	0.19	0.18	0.29	0.15	0.17
MgO	8.36	6.62	7.42	7.36	6.03	6.70	7.80	6.92	5.79	6.94	14.16	6.17	6.25	5.96	13.42	7.21	7.95
CaO	8.15	7.72	7.64	8.06	7.91	7.35	7.54	7.82	8.38	7.73	6.79	8.05	8.52	7.73	6.42	5.18	6.07
Na_2O	2.30	2.75	3.62	2.82	3.24	2.67	2.70	2.86	2.86	2.43	1.54	3.06	2.96	3.18	1.51	4.77	4.11
K_2O	1.48	1.90	0.66	0.69	0.88	1.01	0.57	0.63	0.61	0.64	0.37	0.70	0.57	0.64	0.35	0.98	1.15
P_2O_5	0.18	0.18	0.20	0.21	0.20	0.23	n.a.	n.a.	n.a.	0.20	0.14	0.21	0.21	0.20	0.13	0.13	0.14
LOI	2.95	2.30	2.15	2.84	2.21	2.56	2.71	2.65	2.68	4.55	2.73	2.75	2.47	2.74	8.31	2.31	4.63
LOIc	3.71	2.97	2.94	3.58	2.89	3.54	3.54	3.36	2.68	5.20	3.52	3.50	3.24	3.44	9.58	3.03	5.39
SUM	99.38	98.89	100.06	98.53	99.45	100.38	98.53	98.83	97.85	99.90	99.72	99.80	99.97	99.95	100.06	100.41	99.59
Trace elements (ppm)																	
Rb	41	49	20	32	33	41	23	24	25	29	20	18	16	18	17	31	32
Sr	185	199	141	198	206	129	139	198	245	226	238	252	252	260	81	160	165
Y	51	47	58	57	55	64	53	53	54	56	57	58	59	55	33	41	40
Zr	161	156	173	176	167	204	161	155	161	173	174	173	176	167	146	120	129
Nb	2	3	4	4	4	4	3	3	4	4	4	3	5	5	3	2	3
V	371	393	421	397	408	482	338	370	401	402	422	439	441	414	411	358	369
Cr	213	233	151	239	247	193	315	313	295	244	226	210	220	310	137	123	157
Co	44	52	43	37	52	44	42	43	49	43	44	42	45	49	57	44	40
Ni	71	63	66	74	61	58	88	80	62	56	60	54	58	62	83	56	59
Cu	133	388	18	819	701	92	181	712	69	42	1096	315	108	90	89	221	337
Zn	97	99	112	106	110	126	116	108	113	113	111	116	116	111	169	81	92
Ba	470	617	110	75	114	214	72	90	108	82	104	90	76	83	46	175	212

*: sample used to calculate a mean composition of the least altered zones for diagrams of Grant.
**: sample used to calculate a mean composition of the most altered zones for diagrams of Grant.
O: outer part, amphibole-rich green zone.
G: extremely green part.
B: brown zone.
I: inner part.
Int: intermediate zone between red zone and outer zone.
M: mix between red and green material (difficult to separate).
A, MA: see text for definition.

Table 7
Average composition with standard deviation (s.d.) of basalts from the Solund-Stavfjord Ophiolite Complex (SSOC) and of the least altered (P), the altered (A) and the most altered (MA) basalts from the Solund basin.

Group	SSOC		P		A		MA	
Major elements (wt.%)	Average	s.d.	Average	s.d.	Average	s.d.	Average	s.d.
SiO_2	47.95	1.03	47.85	0.50	48.11	0.72	45.82	5.23
TiO_2	2.46	0.34	2.89	0.44	2.51	0.18	2.24	0.29
Al_2O_3	13.75	0.71	13.06	0.91	13.29	0.38	14.35	0.38
Fe_2O_3T	13.97	1.21	14.89	1.52	13.94	0.72	14.04	2.31
Fe_2O_3	4.14	0.81	3.91	0.83	6.49	1.16	5.78	2.45
FeO	8.78	1.24	9.73	1.83	6.68	0.68	7.42	1.81
MnO	0.22	0.03	0.23	0.03	0.19	0.03	0.21	0.06
MgO	6.61	0.62	5.72	0.48	6.79	0.69	8.73	3.53
CaO	10.47	1.45	9.45	0.44	7.86	0.51	6.97	1.19
Na_2O	2.61	0.62	2.74	0.54	2.93	0.38	3.02	1.21
K_2O	0.10	0.07	0.22	0.07	0.86	0.39	0.68	0.30
P_2O_5	0.26	0.10	0.24	0.05	0.21	0.02	0.17	0.04
LOI	2.02	0.58	3.05	0.68	3.41	0.51	4.53	2.36
Total	99.85	0.92	99.48	0.30	99.39	0.62	99.93	0.27
Trace elements (ppm)								
Rb	1	2	13	6	30	10	22	7
Sr	142	37	141	37	190	35	201	68
Y	62	11	64	9	56	5	49	11
Zr	172	33	202	37	174	16	155	23
V	402	39	473	57	402	30	408	32
Co	55	9	44	5	45	5	46	6
Ni	70	16	62	45	63	9	62	10
Zn	125	28	111	18	115	13	114	28

the basaltic rocks can be recognized from increasingly higher initial (t = 385 Ma) Sr isotopic ratios of the altered clasts.

5. Discussion

5.1. Model of alteration

5.1.1. A coupled mineralogical/chemical model

Based on the mineralogical, chemical and isotopic studies, we propose a model of alteration. This model is based on the hypothesis, in agreement with the Sr isotopic constraints, that the same fluid altered both the basaltic and the ultramafic clasts, in Devonian times shortly after sedimentary deposition. Beinlich et al. (2010) have shown that the ultramafic clasts are strongly altered with MgO removal creating a porosity which is then filled with carbonate and quartz. Most of this alteration occurred during weathering and subsequent interaction between clasts and the basinal fluids during burial in the basin. In the proposed model, alteration occurs at two scales, with chemical exchanges between the ultramafic and the basaltic clasts and between the alteration zones in the basaltic clast.

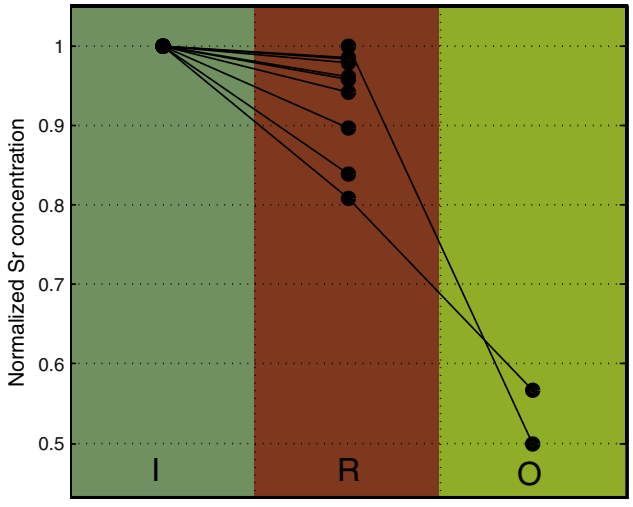

Fig. 8. Evolution of the Sr concentration in 10 samples from the inner green zone (I), to the red zone (R) then to the outer green zone (O). The concentration is normalized to the concentration in I for an easier comparison between the samples. Note that the Sr content systematically decreases from I to O.

At the conglomerate scale, the basaltic clasts lost Ca and acquired Mg whereas, in the meantime, ultramafic clasts incorporate Ca and release Mg. At the boulder scale, a fluid migration inwards from the boulder boundaries or from the fractures is responsible for the basaltic clasts alteration. This fluid interacts with the rock and progressively induces reactions having consequences on the chemistry of the rock.

In the least altered green core of basaltic boulders, both replacement of clinopyroxene by chlorite and alteration of calcite induce a CaO release. This component then escapes from the boulders with the fluid or is reprecipitated locally, by the formation of titanite at the expense of titanohematite. This last reaction also releases FeO which can be partly used in the reactions leading to chlorite formation. An increase in the K_2O content related to the formation of potassium phases (K-feldspar and muscovite) in fractures also occurs.

In the red zones progressively replacing the green cores of basaltic clasts, hematite forms along cracks and/or in aggregates with quartz. Iron is provided by the fluid and by the formation of titanite at the expense of titanomagnetite in the green core. Even though it was not directly observed, the formation of aggregates of quartz and hematite could be a consequence of the removal of calcite in the least altered zone. Indeed, this removal could create a porosity which is then filled by quartz. The formation of large amounts of amphibole is responsible for the enrichment of the system in MgO. Two different kinds of texture are associated to amphiboles. Some amphiboles are zoned and grow in contact with chlorite (Fig. 7d) whereas other amphiboles seem to grow independent of the presence of chlorite. The zonation of the amphiboles surrounding chlorite indicates a change in alteration products with time. First, Fe-rich amphibole replaces chlorite. That process releases MgO which may be used to produce other amphiboles. Whole rock analyses reveal that MgO also was introduced in the clasts and was used to form amphibole. Following our Gresens' analysis (Eq. (3)), FeO also needs to be added to form amphibole. A potential source of iron is the removal of hematite in the green zones. Thus, the replacement of red zones by another green zone could be linked to the

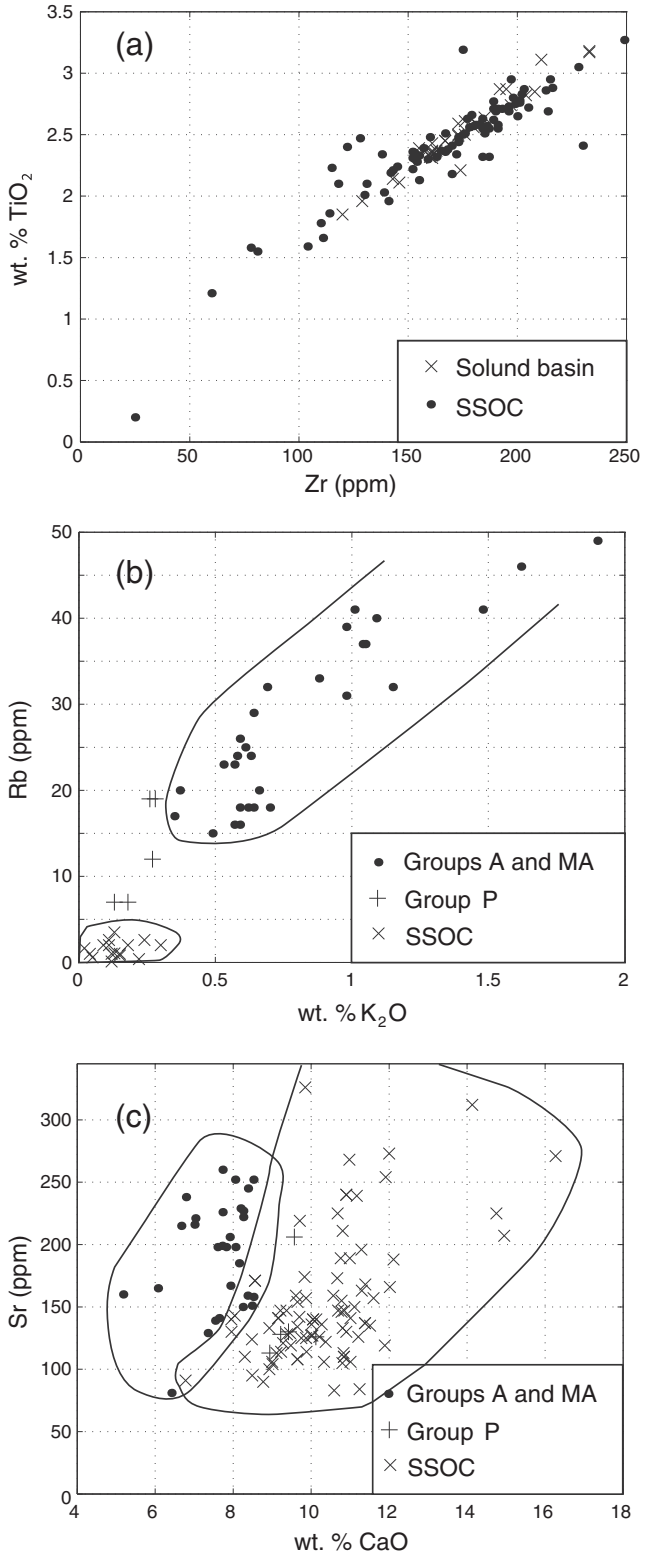

Fig. 9. Plots of compositions of basalts from the SSOC (data from Furnes et al. (1982), Furnes et al. (1990), Ryttvad et al. (2000) and Fonneland-Jørgensen et al. (2005)) and from the Solund basin (this study). (a): Zr content versus TiO_2 content. No distinction can be made between the samples of the SSOC and of the Solund basin. Note the alignment of the data suggesting a positive correlation of magmatic origin. (b): K_2O content versus Rb content. Two different groups are observed with composition of basalts of the least altered group (group P) sitting at the boundary between the basalts of the SSOC and of the Solund basin. Rb is drastically enriched in some altered rocks. (c): CaO content versus Sr content. Two different groups are again separated with basalts of group P at the boundary between the groups.

consumption of iron to produce amphibole. The release of Al_2O_3 when amphibole formed at the expense of chlorite could also explain the formation of albite sometimes observed in the green zone.

5.1.2. Formation and inward migration of the red zones: a mechanism

In the basaltic clasts of the Solund basin, hematite reddened zones form along clast boundaries (Fig. 2) and along fractures that are oriented at high angle to the boundaries of the clasts. The boundary-parallel zones migrate towards the center of the clasts and the fracture-parallel zones migrate away from the fractures. Amphibole-rich green zones can replace these reddened migrating zones. Through this process the clasts develop compartment structures but also more complex pattern of red zones. This evolution has been shown to be related to the deformation of the clasts. The deformation of the clasts may be related to external forces (load of the sediments or tectonic forces) or internal forces caused by reaction induced volume changes or force of crystallization (Fletcher and Merino, 2001).

The concentric distribution of the red zones in Type 1 clasts suggests that they started to form as a result of a reaction between fluid and clast (Fig. 2b). Several generations of cracks are observed. The origin of the first generation of cracks is difficult to assess but may have formed to accommodate stresses resulting from overburden. The following generations of cracks are hierarchically organized (Fig. 5) and we suggest that they were formed in tandem with and certainly as a consequence of progressively locally generated stresses. Alteration zones formed by a deformation-assisted mechanism in which, in particular, oblique fractures were formed indicating an accommodation of a change in volume (Figs. 4 and 5). Thus, generation of local stresses may be due to volume changes caused by reactions in the rock. Alteration-related reactions produced hydrated minerals with higher volume than the original magmatic minerals, for reasons of the gain and loss of elements during reactions (see Gresens' analysis, Eqs. (1), (2), (3) and (4)). However, it is difficult to directly connect the reactions to specific volume changes. Similar volume-change-induced crack formations have however been described in other systems: during serpentinization of ultramafic rocks (Iyer et al., 2008), during mineral replacement reactions (Putnis et al., 2007) or during spheroidal weathering (Fletcher et al., 2006; Røyne et al., 2008).

To understand the physical laws which control the alteration, we compared the results of a numerical modeling which couples diffusion, reaction and deformation (Malthe-Sørenssen et al., 2006 — Fig. 11) to alteration features of our samples. We modeled the alteration of a rock matrix in contact with a fluid. Fluid diffuses into the rock which reacts, resulting in a volume change in that rock. The induced volume change builds up stress which fractures the rock when it reaches a critical value. Fractures then act as fluid channels propagating the diffusion and reaction processes inwards.

Numerical simulation (Fig. 11) provides an evolutionary sequence of alteration processes that can be qualitatively compared to our observations in the samples. First, a clast/block is altered at its boundary by a diffusion process (Fig. 11a). This produces an alteration halo following the boundary of the block. Boulders of Type 1 display the same kind of haloes with concentrically arranged red zones (Fig. 2b). Then, fractures remove the sharp corners (Fig. 11b). This may be observed with sample SOL43-04 where an oblique finger-shaped fracture occurs close to a corner (Fig. 3a and b). Then, fractures can divide the block into two pieces which then can be fragmented by other fractures (Fig. 11c). This hierarchical fracturing is also observed in our samples where different generations of cracks can be identified in samples of Types 2 and 3 (Figs. 4a and b and 5). Two walls located at the upper and lower boundaries of the simulation do not allow increase of volume in the vertical direction. Consequently, oblique cracks and shear zones are formed to accommodate the volume changes and allow a horizontal displacement of matter (Fig. 11d). These kinds of cracks allowing the accommodation of a change of volume are observed in our samples (Figs. 4a and b and 5). Finally, alteration products totally replace the original clast as

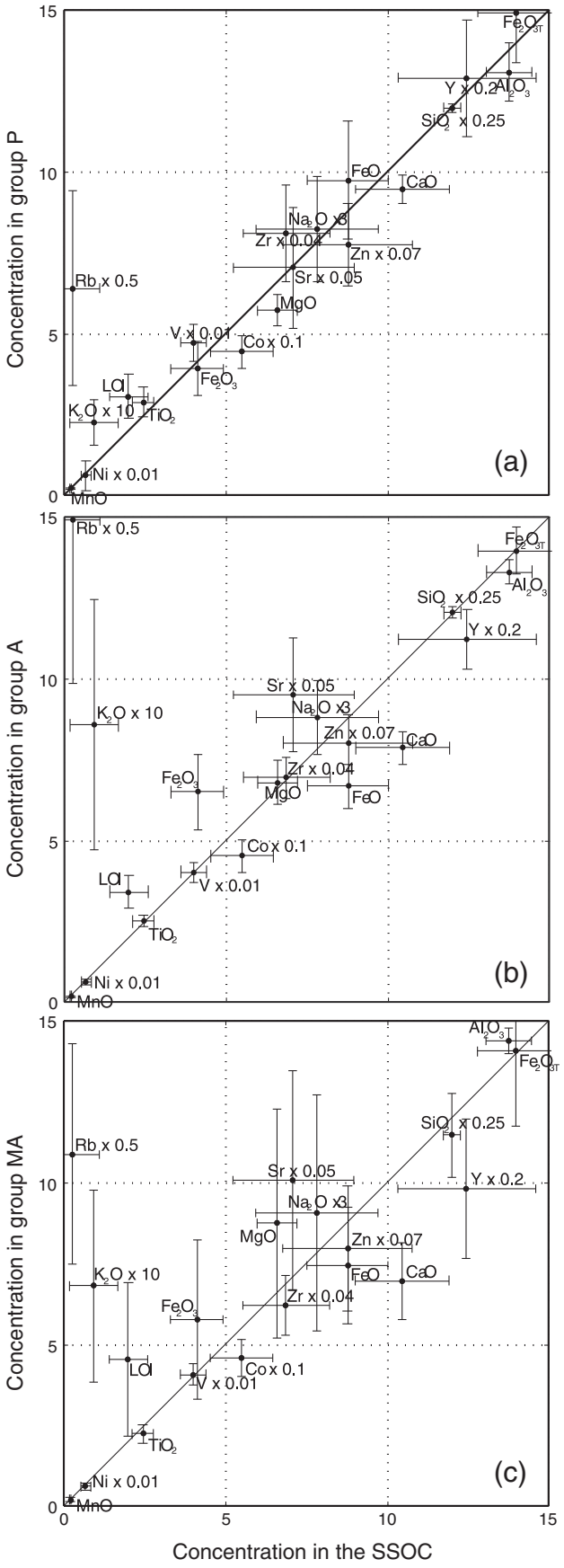

observed in the field with totally brown clasts. Consequently, many similarities are found between the observations and the numerical model. This suggests that a diffusion–reaction process where stresses are generated by a change of volume due to reactions well model the alteration of the clasts. However, it has not been possible to prove with certainty that the mineralogical changes will lead to a volume change. It is therefore not possible to assess the relative importance of external and internal forces. Nevertheless, hydration reactions (like hydration of magmatic pyroxene) combined with the conversion of magmatic assemblages of basalt to low-grade, low-pressure metamorphic assemblages of altered clasts with their typically lower densities indicate that an expansion at least of certain minerals of basaltic clasts during alteration is likely, at least for the early stages of alteration.

Formation of alteration haloes along fractures has already been described in magmatic rocks altered on the oceanic sea-floor (Alt et al., 1998; Alt and Teagle, 2003) or during spheroidal weathering (Fletcher et al., 2006) but the involved mineralogy was different from what is seen in our study. Reddening associated with formation of Fe-oxides in basalt has also been observed (Burkhard and Müller-Sigmund, 2007) but in subaerial basaltic flows and on a scale of only a few millimeters. Thus, the alteration described here has not been studied before and shows the involvement of complex deformation-related alteration processes during burial of multi-components systems. These processes induce changes in many chemical and physical rock properties which have to be acknowledged if a basin and its resources are to be explored or used. Similar processes are involved in other rocks and in other conditions as suggested by observations at hydrothermal conditions (Alt et al., 1998; Alt and Teagle, 2003) and during spheroidal weathering (Fletcher et al., 2006). This suggests that the fundamental physical laws governing the alteration are the same in these very different contexts.

Consequently, this study shows that processes completely different from the dissolution/cementation processes which were described in simple systems can be involved in multicomponent systems. They have an impact on the chemical and physical properties of the rocks which must be kept in mind in basin studies and in particular in basin modeling. The 'reactive compaction' we see in the multicomponent Solund basin clast system redistributes elements between clasts, changes the rock densities on a mineral to clast scale and possibly also on larger scales, and may affect the permeability of the rocks by inducing fracturing and formation of secondary porosity.

5.2. Geological environments for the alteration events

Like the peridotite clasts of the Solund basin (Beinlich et al., 2010), the basaltic clasts may have been altered in three potential settings: 1) hydrothermal alteration on the sea-floor 2) during weathering and transport from their source to the basin 3) during burial in the basin. Fonneland-Jørgensen et al. (2005) reported on hydrothermal alteration in the SSOC. Higher K_2O values in the altered rocks than in the unaltered rocks (with a maximum of 0.3 wt.%) are characteristic of the hydrothermal alteration observed in the SSOC. The mean content of K_2O in our samples is ~0.7 wt.% with a maximum of 1.9 wt.%. The enrichment in K_2O linked to hydrothermal alteration in the ophiolite is thus much smaller than the enrichment observed in our samples. Instead, elevated K_2O contents more likely are due

Fig. 10. Isocon diagram of Grant (2005) comparing average composition of basalt from the SSOC and average composition of (a) the least altered (group P), (b) the altered (group A) and (c) the most altered (group MA) basalts from the Solund basin (see Table 7 for compositions used here). Error bars are plotted by using the calculated standard deviation (Table 7). Some elements have been scaled to display a better dispersion of the points (multiplication factors are indicated). SiO_2, TiO_2, Al_2O_3, Fe_2O_{3T} Fe_2O_3, FeO, MnO, MgO, CaO, Na_2O, K_2O and LOI are expressed in wt.% and Rb, Sr, Y, Zr, V, Co, Ni and Zn in ppm. Black line refers to same compositions in the SSOC and in the basaltic clasts. Note the increase in K_2O, Fe_2O_3, volatiles contents and Rb and the decrease in CaO and FeO during the alteration.

Table 8
Rb/Sr data of the investigated samples.

Sample	Rb (ppm)	Sr (ppm)	$^{87}Rb/^{86}Sr$	$^{87}Sr/^{86}Sr$ measured	$^{87}Sr/^{86}Sr$ $2\sigma_m$ [%]	$^{87}Sr/^{86}Sr$ at 385 Ma
SOL30-08JG (chlorite-like)	8.94	74.5	0.347	0.712182	0.0012	0.710279 ± 0.000053
SOL30-08I2I(2) (green inner part)	16.1	310	0.150	0.708439	0.0012	0.707615 ± 0.000039
SOL30-08I2R (internal red zone)	13.9	257	0.157	0.708110	0.0013	0.707250 ± 0.000039
SOL30-08I2R (red outer part)	16.9	250	0.196	0.708470	0.0014	0.707394 ± 0.000041
SOL43-04O (brown rim of clast)	19.1	202	0.273	0.708735	0.0012	0.707236 ± 0.000047
SOL43-04R (red part of clast)	22.5	245	0.266	0.708613	0.0014	0.707156 ± 0.000046
SOL43-04I2 (inner green part)	24.0	316	0.220	0.708434	0.0012	0.707228 ± 0.000043
SOL43-04I1 (rim of inner green part)	26.5	247	0.310	0.708951	0.0013	0.707249 ± 0.000050

Errors are reported at the 2σ level. An uncertainty of ± 1.5% is assigned to Rb/Sr ratios.
Errors for $^{87}Sr/^{86}Sr(t)$ include error magnification and a standard error of ± 0.005% for measured $^{87}Sr/^{86}Sr$ data.

to K acquisition from intrabasinal diagenetic fluids. Elevated $^{87}Sr/^{86}Sr$ ratios in these fluids (see above) suggest that Sr was released to these fluids to a major extent from K, Rb-rich phases of the old continent-derived detritus in the basin. Release of radiogenic Sr from such phases would also lead to release of major amounts of K to the fluids, which would explain the here observed incorporation of considerable amounts of K into the meta-basaltic alteration assemblages. Moreover, in all the studied samples, alteration follows the spheroidal shape of the boulder with alteration haloes parallel to the surface. Such spheroidal boulders have probably been formed in a continental environment and transported towards the basin by river flood events. Consequently, the observed alteration can only to a minor degree result from hydrothermal alteration on the ocean floor.

As to the potential weathering-related alteration, plate tectonic reconstructions place Scandinavia in a near equatorial position in Lower Devonian time (Torsvik et al., 2005). Continental near-surface weathering at tropical conditions during the Devonian may have promoted the alteration of the clasts. Alteration of basalts at near-surface conditions has been studied in great detail (Eggleton et al., 1987; Moon and Jayawardane, 2004; Sak et al., 2004, 2010; Navarre-Sitchler et al., 2011). Al-hydroxides and/or clays are typically formed during alteration in this context. We do not observe these minerals in our samples. So it seems that the observed alteration is not a result of a continental subaerial alteration. Instead, the relationships between the boulders and the matrix suggest that alteration occurs during compaction. Alteration reddening which preferentially propagates from an indentation point between two boulders and deformed samples that are foliated and strongly altered because of the compaction are sometimes observed. Sr isotopes show that the chemistry in the alteration zones of the basaltic clasts is dominantly impacted by interaction with the fluids of the basin. Consequently, the intrabasinal alteration appears to be the dominant stage of alteration of the clasts.

Moreover, the studied samples typically contain chlorite, epidote, albite and actinolite which are minerals commonly formed at low-grade metamorphic conditions, in greenschist facies (Spear, 1993). The typical range of temperature associated with this metamorphic facies is of 250–500 °C. These temperatures can be reached in hydrothermal systems (where similar alteration assemblages can be observed; Teagle and Alt, 2004) but also during the deep burial of sediments and in particular during the burial in the Solund basin (Svensen et al., 2001). In that case, the artificial boundary between diagenesis and metamorphism is exceeded. That involves complex chemical and physical mechanisms that are probably common in basin undergoing deep burial due to the reached conditions.

The modal composition of the basaltic rocks of the Solund-Stavfjord Ophiolite Complex (Furnes et al., 1982, 1990; Ryttvad et al., 2000; Fonneland-Jørgensen et al., 2005; Furnes et al., 2006) is similar to the composition of the least altered samples of the basaltic clasts described here. The above authors described greenschist facies alteration assemblages in some basalts of the SSOC and proposed that this overprint may be due to an ocean-floor alteration. However, as the conglomerate of the Solund basin rests on this ophiolite, the origin of the alteration assemblages found in the SSOC could be just the same as the origin of the alteration assemblages described in the studied samples. Consequently,

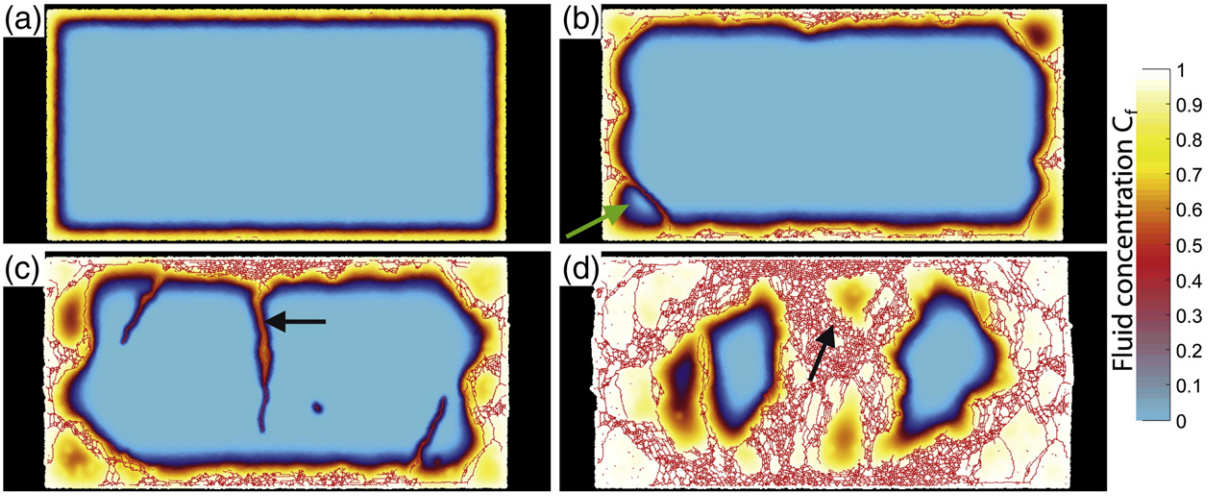

Fig. 11. 4 successive results of the diffusion–reaction model (Malthe-Sørenssen et al., 2006) showing the normalized fluid concentration (the proportion of fluid compare to rock) during the progressive alteration (from (a) to (d)) of a rock in two dimensions. Fractures are represented by red lines. (a): the rock is first altered by diffusion at its boundary. (b): The corners (green arrow) are spalled and rapidly altered. (c): Apparition of a main crack at right angle to the boundary (arrow) propagating the fluid inwards. (d): The rock is quite completely altered with only three unaltered compartments remaining. Note the presence of numerous oblique cracks and shear zones due to the external boundaries in the final dense network of cracks (arrow).

an alternative hypothesis could be that the rocks of the SSOC were altered in the greenschist facies as a consequence of increased pressures and temperatures during subsidence of the basin above.

5.3. Compaction by exchange of CaO and MgO between basaltic and peridotitic clasts

Beinlich et al. (2010) found that material located close to peridotite clasts is enriched in MgO derived from the peridotite. Notably amphiboles show ongrowth of Mg-rich rims similar to those reported here for the basaltic clasts. The formation of abundant calcite induces a strong enrichment in CaO in the altered peridotite (from ~1 wt.% in the least altered sample to ~30 wt.% in the carbonatized clasts) due to formation of abundant calcite. Sr isotope data indicate that the calcite formed from basinal brines and not from seawater. The removal of CaO from the basaltic clasts suggests that they may have acted as a Ca-source and that the two clast types (basaltic and ultramafic) exchanged matter during burial and compaction. It is likely that other clast lithologies may also have interacted since the K_2O increase in the basalt may require a K_2O source, like K-feldspar or mica phases from granite clasts. It appears that basin fills of multicomponent clast populations compact through internal, complex chemical exchange mechanisms involving partial equilibration between the compositions of the different clasts. This process involves consumption of fluid components, growth of new minerals, at least local volume changes due to mineral reactions, and consequently the build-up of stress which then promotes progressive fracturing and further reaction progress.

5.4. CO_2 sequestration in basalts and peridotites

We notice that while the peridotitic clasts of the Solund basin are strongly carbonated, with formation of abundant calcite, the basaltic material contains only minor amounts of carbonate. However, our work suggests that the basalt plays an important role as a provider of CaO for the carbonation of the peridotite. When multiple zones occur in basaltic clasts, an outermost green zone can be present. Amphibole is formed in this Mg-rich zone and not the CO_2-sequestering phases calcite or magnesite, which are found in the ultramafic clasts (Beinlich et al., 2010). Consequently, CO_2 appears to be sequestered, in the here given system, much easier in ultramafic than in basaltic clasts. This preferential sequestration is perhaps linked to the development of local chemical environments around the clasts as suggested by Hövelmann et al.(2011).

6. Conclusions

1. We show that combined deformation/reaction processes are responsible for the alteration of the basaltic clasts of Solund basin. Volume changes caused by the reaction of the rock induce the formation of hierarchical cracks. These deformation features allow fluid propagation inwards and consequently to further propagate the alteration into the clasts. Reaction progress in this multi-component clast system therefore is self-sustaining or may even be described as a runaway process.
2. Red zones associated with hematite form along the cracks. In these red zones, primary minerals react to form minerals of the greenschist facies (chlorite, epidote and amphibole). Then, amphibole-rich green zones progressively replace these red zones. This shows that reactions proceed not directly from an unaltered to a 'final' stage but that several intermediate product assemblages may be formed.
3. The comparison of the immobile element contents in our samples with those of the adjacent Solund Stavfjord Ophiolite Complex shows that basaltic clasts probably originate from this ophiolite. The intrabasinal alteration of the basaltic clasts involves an oxidation of the rock, a loss of CaO and a gain of MgO and K_2O. Namely the gain in K_2O and MgO demonstrates that also K-bearing phases (possibly detrital mica) and Mg-rich clasts (ultramafic clasts) take part in the reactive compaction process.
4. At the basin scale, high strontium isotope ratios show that basaltic and ultramafic boulders were mainly altered by the same fluid. The loss of CaO and the gain of MgO in the basaltic clasts appear to be coupled with the loss of MgO and the gain of CaO in the ultramafic clasts. Basaltic clasts are moderately altered whereas strong chemical changes occur in the ultramafic clasts. Notably, CO_2 sequestration appears to be much more efficient in the ultramafic clasts.
5. The here documented reactive compaction process in a multicomponent clastic system differs from classical pressure solution-reprecipitation compaction and cementation mechanisms seen in more primitively composed sediments like sandstones. The here involved redistribution of elements may alter the textural, mineralogical and physical characteristics of original clasts to beyond recognition.

Acknowledgments

We are grateful to Melanie Barnes, Texas Tech for providing the FeO titration data. Muriel Erambert and Turid Winje guided the EMP analyses and XRF work, respectively. Financial support to PGP from NFR is acknowledged. The work was carried out during the first author's internship period at PGP. We thank Johan Petter Nystuen for valuable comments and discussion and two anonymous reviewers for their insightful suggestions. Field-company and discussion with Torgeir B. Andersen, Andreas Beinlich, Jørn Hövelmann and Alban Souche are greatly appreciated. Anaïs Aubert is acknowledged for help with the figures.

References

Alt, J.C., Teagle, D.A.H., 2003. Hydrothermal alteration of upper oceanic crust formed at a fast-spreading ridge: mineral, chemical and isotopic evidence from ODP Site 801. Chemical Geology 201, 191–211.
Alt, J.C., Teagle, D.A.H., Brewer, T., Shanks III, W.C., Halliday, A., 1998. Alteration and mineralization of an oceanic forearc and the ophiolite-ocean crust analogy. Journal of Geophysical Research 103, 12365–12380.
Audet, D.M., Fowler, A.C., 1992. A mathematical model for compaction in sedimentary basins. Geophysical Journal International 110, 577–590.
Bakke, S., Øren, P.-E., 1997. 3-D pore-scale modelling of sandstones and flow simulations in the pore networks. SPE Journal 2, 136–149.
Beinlich, A., Austrheim, H., Glodny, J., Erambert, M., Andersen, T.B., 2010. CO_2 sequestration and extreme Mg depletion in serpentinized peridotite clasts of the Devonian Solund Basin, SW-Norway. Geochimica et Cosmochimica Acta 74, 6935–6964.
Benson, L.V., Teague, L.S., 1982. Diagenesis of basalts from the Pasco basin, Washington. I. Distribution and composition of secondary mineral phases. Journal of Sedimentary Petrology 52, 595–613.
Bernabé, Y., Evans, B., 2007. Numerical modelling of pressure solution deformation at axisymmetric asperities under normal load. Geol. Soc. London Spec. Publi. 284, 185–205.
Bohn, S., Douady, S., Couder, Y., 2005a. Four sided domains in hierarchical space dividing patterns. Physical Review Letters 94, 1–4.
Bohn, S., Pauchard, L., Couder, Y., 2005b. Hierarchical crack pattern as formed by succesive domain division. I. Temporal and geometrical hierarchy. Physical Review E 71, 1–7.
Burkhard, D.J.M., Müller-Sigmund, H., 2007. Surface alteration of basalt due to cation-migration. Bulletin of Volcanology 69, 319–328.
David, C., Menendez, B., Zhu, W., Whong, T.-F., 2001. Mechanical compaction, microstructures and permeability evolution in sandstones. Physics and Chemistry of the Earth 26, 45–51.
Dickinson, W.W., Milliken, K.L., 1995. The diagenetic role of brittle deformation in compaction and pressure solution, Etjo sandstone, Namibia. Journal of Geology 103, 339–347.
Eggleton, R.A., Foudoulis, C., Varkevisser, D., 1987. Weathering of basalt: changes in rock chemistry and mineralogy. Clays and Clay Minerals 35, 161–169.
Fletcher, R.C., Merino, E., 2001. Mineral growth in rocks: kinetic-rheological models of replacement, vein formation, and syntectonic crystallization. Geochimica et Cosmochimica Acta 65, 3733–3748.
Fletcher, R.C., Buss, H.L., Brantley, S.L., 2006. A spheroidal weathering model coupling porewater chemistry to soil thicknesses during steady-state denudation. Earth and Planetary Science Letters 244, 444–457.
Fliegel, D., Wirth, R., Simonetti, A., Schreiber, A., Furnes, H., Muehlenbachs, K., 2011. Tubular textures in pillow lavas from a Caledonian west Norwegian ophiolite: a combined TEM, LA-ICP-MS, and STXM study. Geochemistry, Geophysics, Geosystems 12, 1–21.

Fonneland-Jørgensen, H., Furnes, H., Muehlenbachs, K., Dilek, Y., 2005. Hydrothermal alteration and tectonic evolution of an intermediate- to fast-spreading back-arc oceanic crust: Late Ordovician Solund-Stavfjord ophiolite, western Norway. Island Arc 14, 517–541.
Furnes, H., 1974. Structural and metamorphic history of the Lower Paleozoic metavolcanics and associated sediments in the Solund area, Sogn. Norges Geologiske Undersokelse Bulletin 302, 33–74.
Furnes, H., Thon, A., Nordas, J., Garmann, L.B., 1982. Geochemistry of Caledonian metabasalts from some Norwegian Ophiolite fragments. Contributions to Mineralogy and Petrology 79, 295–307.
Furnes, H., Skjerlie, K.P., Pedersen, R.B., Andersen, T.B., Stillman, C.J., Suthren, R.J., Tysseland, M., Garmann, L.B., 1990. The Solund-Stavfjord Ophiolite Complex and associated rocks, west Norwegian Caledonides: geology, geochemistry and tectonic environment. Geological Magazine 127, 209–224.
Furnes, H., Skjerlie, K.P., Dilek, Y., 2000. Petrology, tectonics, and hydrothermal alteration of a fossil backarc oceanic crust: Solund-Stavfjord ophiolite complex of the western Norwegian Caledonides: A review. In: Dilek, Y., Moores, E.M., Elthon, D., Nicolas, A. (Eds.), Ophiolites and Oceanic Crust: New Insights from Field Studies and the Ocean Drilling Program. Geol. Soc. of Am, Boulder, Colo, pp. 443–460.
Furnes, H., Hellevang, B., Hellevang, H., Robins, B., 2006. Evolution of lavas in the late Ordovician/Early Silurian Solund-Stavjord Ophiolite Complex, West Norway. Geochemistry, Geophysics, Geosystems 7, 1–32.
Gale, G.H., Roberts, D., 1974. Trace element geochemistry of Norwegian Lower Paleozoic basic volcanics and its tectonic implications. Earth and Planetary Science Letters 22, 380–390.
Gislason, S.R., Wolff-Boenisch, D., Stefansson, A., Oelkers, E.H., Gunnlaugsson, E., Sigurdardottir, H., Sigfusson, B., Broecker, W.S., Matter, J.M., Stute, M., Axelsson, G., Fridriksson, T., 2010. Mineral sequestration of carbon dioxide in basalt: a preinjection overview of the CarbFix project. International Journal of Greenhouse Gas Control 4, 537–545.
Grant, J.A., 2005. Isocon analysis: a brief review of the method and applications. Physics and Chemistry of the Earth 30, 997–1004.
Gresens, R.L., 1967. Composition-volume relationships of metasomatism. Chemical Geology 2, 47–65.
Gysi, A.P., Stefánsson, A., 2011. CO_2-water–basalt interaction. Numerical simulation of low temperature CO_2 sequestration in basalt. Geochimica et Cosmochimica Acta 75, 4728–4751.
Hacker, B.R., Andersen, T.B., Root, D.B., Mehl, L., Mattinson, J.M., Wooden, J.L., 2003. Exhumation of high-pressure rocks beneath the Solund Basin, Western Gneiss Region of Norway. Journal of Metamorphic Geology 21, 613–629.
Hickman, S.H., Evans, B., 1995. Kinetics of pressure solution at halite-silica interfaces and intergranular clay films. Journal of Geophysical Research 100, 13113–13132.
Horváth, Z., Varga, B., Mindszenty, A., 2000. Micromorphological and chemical complexities of a lateritic profile from basalt (Jos Plateau, Central Nigeria). Chemical Geology 170, 81–93.
Hossack, J.R., 1984. The geometry of listric faults in the Devonian basins of Sunnfjord W. Norway. Journal of the Geological Society of London 141, 629–637.
Hossack, J.R., Cooper, M.A., 1986. Collision tectonics in the Scandinavian Caledonides. In: Coward, M.P., Ries, A.C. (Eds.), Collision Tectonics: Geol. Soc., Spec. Public., 19, pp. 287–304.
Hövelmann, J., Austrheim, H., Beinlich, A., Munz, I.A., 2011. Experimental study of the carbonation of partially serpentinized and weathered peridotite. Geochimica et Cosmochimica Acta 75, 6760–6779.
Howarth, R.J., McArthur, J.M., 1997. Statistics for strontium isotope stratigraphy: a robust LOWESS fit to the marine strontium isotope curve for the period 0 to 206 Ma, with look-up table for the derivation of numerical age. Journal of Geology 105, 441–456.
Indrevær, G., Steel, R.J., 1975. Some aspects of the sedimentary and structural history of the Ordovician and Devonian rocks of the westernmost Solund Islands, West Norway. Norges Geologiske Undersokelse Bulletin 317, 23–32.
Iyer, K., Jamtveit, B., Mathiesen, J., Malthe-Sørenssen, A., Feder, J., 2008. Reaction-assisted hierarchical fracturing during serpentinization. Earth and Planetary Science Letters 267, 503–516.
Kelemen, P.B., Matter, J., 2008. In situ carbonation of peridotite for CO_2 storage. Proceedings of the National Academy of Sciences of the United States of America 105, 17295–17300.
Kolderup, C.F., 1926. Hornelens Devonfelt. Bergnes Mus. Naturvidensk Rekke, 6. AARB.
Kretz, R., 1983. Symbols for rock-forming minerals. American Mineralogist 68, 277–279.
Labrousse, L., Jolivet, L., Andersen, T.B., Agard, P., Maluski, H., Scharer, U., 2004. Pressure–temperature–time–deformation history of the exhumation of ultra-high pressure rocks in the Western Gneiss Region, Norway. Geological Society of America Special Paper 380, 155–183.
Lander, L.H., Walderhaug, O., 1999. Predicting porosity through simulating sandstone compaction and quartz cementation. AAPG Bulletin 83, 433–449.
Liesegang, R.E., 1913. Geologische Diffusionen. Theodor Steinkopff, Dresden Leipzig. 180 pp.
Liesegang, R.E., 1915. Die Achate. Theodor Steinkopff, Dresden Leipzig. 120 pp.
Malthe-Sørenssen, A., Jamtveit, B., Meakin, P., 2006. Fracture patterns generated by diffusion controlled volume changing reactions. Physical Review Letters 96, 1–4.
McArthur, J.M., Howarth, R.J., Bailey, T.R., 2001. Strontium isotope stratigraphy: LOWESS Version 3. Best-fit line to the marine Sr-isotope curve for 0 to 509 Ma and accompanying look-up table for deriving numerical age. Journal of Geology 109, 155–169.
Moon, V., Jayawardane, J., 2004. Geomechanical and geochemical changes during early stages of weathering of Karamu Basalt, New Zealand. Engineering Geology 74, 57–72.
Navarre-Sitchler, A., Steefel, C.I., Sak, P.B., Brantley, S.L., 2011. A reactive-transport model for weathering rind formation on basalt. Geochimica et Cosmochimica Acta 75, 7644–7667.
Nilsen, T.H., 1968. The relationship of sedimentation to tectonics in the Solund district of southwestern Norway. Norg. Geol. Unders. B. 259, 1–108.
Ohkawa, M., Yamashita, Y., Inoue, M., Kitagawa, R., Takeno, S., 2000. Hematite in pyrophyllite ore deposits, Shobara district, southwestern Japan. Mineralogy and Petrology 70, 15–23.
Osmundsen, P.T., Andersen, A., 2001. The middle Devonian basins of western Norway: sedimentary response to large-scale transtensional tectonics? Tectonophysics 332, 51–68.
Osmundsen, P.T., Andersen, T.B., Markussen, S., Svendby, A.K., 1998. Tectonics and sedimentation in the hanging wall of a major extensional detachment: the Devonian Kvamshesten Basin, western Norway. Basin Research 10, 213–234.
Ostwald, W., 1925. Zur Theorie der Liesegang'schen Ringe. Colloid & Polymer Science 36, 380–390.
Otake, T., Wesolowski, D.J., Anovitz, L.M., Allard, L.F., Ohmoto, H., 2010. Mechanisms of iron oxide transformations in hydrothermal systems. Geochimica et Cosmochimica Acta 74, 6141–6156.
Pedersen, R.B., Furnes, H., Dunning, G., 1991. A U/Pb age for the Sulitjelma Gabbro, North Norway: further evidence for the development of a Caledonian marginal basin in Ashgill–Landovery time. Geological Magazine 128, 141–153.
Putnis, C.V., Geisler, T., Schmid-Beurmann, P., Stephan, T., Giampaolo, C., 2007. An experimental study of the replacement of leucite by analcime. American Mineralogist 92, 19–26.
Renard, F., Park, A., Ortoleva, P., Gratier, J.-P. Gratier, 1999. An integrated model for transitional pressure soluion in sandstones. Tectonophysics 312, 97–115.
Rosenbauer, R.J., Thomas, B., Bischoff, J.L., Palandri, J., 2012. Carbon sequestration via reaction with basaltic rocks: geochemical modeling and experimental results. Geochimica et Cosmochimica Acta 89, 116–133.
Røyne, A., Jamtveit, B., Mathiesen, J., Malthe-Sørenssen, A., 2008. Controls on rock weathering rates by reaction-induced hierarchical fracturing. Earth and Planetary Science Letters 275, 364–369.
Ryttvad, H.L., Furnes, H., Skjerlie, K.P., Rolfsen, R., 2000. Geochemistry and petrogenesis of extrusive rocks, dykes and high-level plutonic rocks on the island of Oldra, Solund-Stavfjord Ophiolite Complex, western Norway. Norsk Geologisk Tidsskrift 80, 97–110.
Sak, P.B., Fisher, D.M., Gardner, T.W., Murphy, K., Brantley, S.L., 2004. Rates of weathering rind formation on Costa Rican basalt. Geochimica et Cosmochimica Acta 68, 1453–1472.
Sak, P.B., Navarre-Sitchler, A.K., Miller, C.E., Daniel, C.C., Gaillardet, J., Buss, H.L., Lebedeva, M.I., Brantley, S.L., 2010. Controls on rind thickness on basaltic andesite clasts weathering in Guadeloupe. Chemical Geology 276, 129–143.
Schweitzer, E.L., Papike, J.J., Bence, A.E., 1979. Statistical analysis of clinopyroxenes from deep-sea basalts. American Mineralogist 64, 501–513.
Spear, F.S., 1993. Metamorphic phase equilibria and pressure–temperature–time paths. Mineral Soc. Amer. Monograph, 1. MSA, Washington, D.C.
Svensen, H., Jamtveit, B., Banks, D.A., Karlsen, D., 2001. Fluids and halogens at the diagenetic–metamorphic boundary: evidence from veins in continental basins, western Norway. Geofluids 1, 53–70.
Teagle, D.A.H., Alt, J.C., 2004. Hydrothermal alteration of basalts beneath the bent hill massive sulfide deposit, middle valley, Juan de Fuca Ridge. Economic Geology 99, 561–584.
Thomas, W.M., 1982. Stability relations of the amphibole hastingsite. American Journal of Science 282, 136–164.
Torsvik, T.H., Robin, L., Cocks, M., 2005. Norway in space and time: a centennial cavalcade. Norwegian Journal of Geology 85, 73–86.
Wenwu, H., Hajash, A., Sparks, D., 2003. Creep compaction of quartz aggregates: effects of pore-fluid flow. A combined experimental and theoretical study. American Journal of Science 303, 73–93.
Wolff-Boenisch, D., Wenau, S., Gislason, S.R., Oelkers, E.H., 2011. Dissolution of basalts and peridotite in seawater, in the presence of ligands, and CO_2: implications for mineral sequestration of carbon dioxide. Geochimica et Cosmochimica Acta 75, 5510–5525.
Zindler, A., Hart, S., 1986. Chemical geodynamics. Annual Review of Earth and Planetary Sciences 14, 493–571.
Zubtsov, S., Renard, F., Gratier, J.-P., Guiguet, R., Dysthe, D.K., Traskine, V., 2004. Experimental pressure solution compaction of synthetic halite/calcite aggregates. Tectonophysics 385, 45–57.